LUND UNIVERSITY

Development of Techniques for 3D Imaging with Focused Ion Beams - Hydrogen Depth Profiling and Microtomography with Applications in Geology

Wegdén, Marie

2007

[Link to publication](#)

Total number of authors:
1

Development of Techniques for 3D Imaging with Focused Ion Beams

Hydrogen Depth Profiling and Microtomography
with Applications in Geology

Doctoral Thesis

Marie Wegdén

Division of Nuclear Physics
Department of Physics
2007

LUND
UNIVERSITY

Abstract

In nuclear microprobe experiments, high resolution maps of the measured parameter, e.g. element- or mass distribution, in a sample can be produced with a variety of ion beam analytical techniques. The principle underlying all the techniques is that ions at MeV energies are used as projectiles to cause interactions with the target material. Because of the limited range of ions in matter, there is a maximum analytical depth for every sample. This means that either the samples must be restricted to micrometre thickness, or that information can be obtained from only the outer few micrometres of a thick sample.

For samples with complex structure, standard, two-dimensional maps do not always deliver full and satisfactory information. Then the possibility of three-dimensional analysis can offer valuable additional information. This work focuses on techniques for obtaining depth profiles and three-dimensional information, both of element distribution and mass distribution, mainly in geological samples.

A method for depth profiling of hydrogen, with the elastic proton-proton scattering "technique" is described. Due to the detection of protons in coincidence at certain angles, the method is highly specific for hydrogen and offers sensitivity in the ppm region. This makes the method especially suited for the analysis of hydrogen in anhydrous minerals, which contain ppm levels of hydrogen in the bulk, and are difficult to analyse due to the care one has to take not to damage or alterate the sample due to the volatility of hydrogen. The depth profiling capacity of the method is used to study the bulk hydrogen content away from the influence of the ever present surface contamination. Also for the study of zonations in minerals the method is of great importance and benefit.

The second part of the work describes the development of a system for microtomography at the Lund nuclear microprobe. This system is dedicated to the analysis of microscopic samples with complex structures, and can provide information of the mass distribution via scanning transmission ion microscopy technique (STIM) and is well suited for future particle-induced X-ray emisson (PIXE) tomography for qualitative and/or quantitative imaging of the element distribution. Tomographic experiments have been performed on test samples, to determine and optimise experimental parameters and test the reconstruction technique on real experimental data. Also, the tomography system has been used in a study of the porosity in the clay material bentonite. Here it is demonstrated that, in a combination, PIXE, hydrogen analysis and microtomography with the STIM technique, can provide unique information on the internal structure and element distribution in a microscopic sample.

Populärvetenskaplig sammanfattning

Inom jonstråleanalysen används en partikelstråle, vanligtvis av protoner eller alfapartiklar, med hög energi för undersökning av prov. Då dessa partiklar skjuts in i provet sker kollisioner, reaktioner eller annan form av växelverkan med elektroner och kärnor i provets inre. En del av dessa processer ger upphov till högenergetisk strålning som kan studeras med lämpliga detektorer. Ur den information som fångas med detektorerna kan slutsatser dras om provets sammansättning, massfördelning eller koncentrationen av olika grundämnen. Om partikelstrålen fokuseras ner till en storlek runt en tusendels millimeter och flyttas över provet, så att endast en liten area analyseras i taget, kan informationen användas till att skapa kartor över provet. Dessa tvådimensionella kartor har dock den svagheten att de visar den sammanlagda informationen över hela provets tjocklek (eller i vissa fall från provets yta ner till ett visst djup) överlagrat i samma karta, på samma sätt som röntgenbilder inom medicinen. Sådana kartor är svåra att tolka och det är omöjligt att urskilja t.ex. om ett visst grundämne är jämnt fördelat eller om det är speciellt ansamlat på ett specifikt djup i provet. Då kan analysmetoder som möjliggör tredimensionell avbildning vara ett intressant alternativ.

Detta arbete handlar om just utveckling av metoder för att utvinna tredimensionell information ur ett prov. Två helt olika metoder presenteras: en för analys av vätehalten i geologiska prov och en annan för studier av massfördelningen med hjälp av mikrotomografi. Alla experiment har utförts vid Lunds Nukleära Mikrosond, som är ett instrument bestående av en 3 MV Van de Graaff accelerator med tillhörande strålrör med optik för strålfokusering, samt experimentkammare, detektorer och datainsamlingssystem.

Väteanalysen utförs med s.k. proton-protonspridning. En proton skjuts in i ett prov där den kolliderar med en vätekärna (som även den är en proton) och båda dessa sprids ut ur provet och detekteras parvis samtidigt i en specialanpassad tvådelad detektor. Metoden är helt specifik för väte, för om den infallande protonen skulle träffa på en annan kärna än just en vätekärna, så nås detektorn inte av två samtidiga protoner. Metoden har hög känslighet och kan detektera mycket låga koncentrationer av väte, ända ner till ppm-området. Dessutom kan informationen användas för att diskriminera vätekontaminering på provytan från vätekoncentrationen inne i provet.

När vi i vardagslag talar om tomografi, menar vi ofta s.k. skiktröntgen inom medicinen, som används t.ex. vid diagnostik eller för att studera hur människokroppen ser ut inuti. I detta arbete beskrivs design, utveckling och uppbyggnad av ett flexibelt system för jonstråletomografi av mikroskopiska prover. Valet av rekonstruktionsteknik, för att komma åt tredimensionell information från projektionsdata (tvådimensionell information) tagen i många olika vinklar, föll på filtrerad bakåtprojektion, eftersom det är en enkel och snabb metod. Denna metod demonstreras på såväl simulerade som experimentella data över massfördelningen i olika typer av prov.

Slutligen har jag kombinerat väteanalys med tomografi för att studera porositeten i bentonitlera, som ska användas som stötdämpare och barriär då

kopparkapslar med uttjänt bränsle från de svenska kärnkraftverken ska slutförvaras i berggrunden enligt förslag KBS-3 (*KärnBränsleSäkerhet*). Den tredimensionella information som tomografin bidrar med, samt kombinationen av flera jonstrålebaserade mätmetoder, har visat sig vara värdefull i undersökningen av bentonits inre porösa struktur.

Abbreviations

ADC	Analog to digital converter
ART	Algebraic reconstruction technique
CT	Computer(-ised) tomography
DISRA	Discretised Image Space Reconstruction Algorithm
ERDA	Elastic recoil detection analysis
FBP	Filtered backprojection
FSW	Friction stir welding
FTIR	Fourier transform infrared spectroscopy
HLW	High level waste
KBS-3	KärnBränsleSäkerhet (*Nuclear Fuel Safety*)
MRI	Magnetic resonance imaging
NAM	Nominally anhydrous minerals
NIM	Nuclear Instrumentation Module
NMP	Nuclear microprobe
NRA	Nuclear reaction analysis
NRI	Nuclear resonance imaging
PBL	Proton beam lithography
PET	Positron emission tomography
PIXE	Particle-induced X-ray emission
RBS	Rutherford backscattering spectrometry
SCA	Single channel analyser
SIMS	Secondary ion mass spectrometry
SPECT	Single photon emission CT
SRIM	The Stopping and Range of Ions in Matter
STIM	Scanning transmission ion microscopy

List of publications

Papers included in the thesis and the author's contribution.

Paper I **Hydrogen analysis by p-p scattering in geological material**

M. Wegdén, P. Kristiansson, Z. Pastuovic, H. Skogby, V. Auzelyte,
M. Elfman, K.G. Malmqvist, C. Nilsson, J. Pallon, A. Shariff
Nucl. Instr. and Meth. B 219-220 (2004) 550-554.

I planned and carried out the experiment, executed the data evaluation and simulations. I wrote the paper.

Paper II **Hydrogen depth profiling by p-p scattering in nominally anhydrous minerals**

M. Wegdén, P. Kristiansson, H. Skogby, V. Auzelyte, M. Elfman,
K.G. Malmqvist, C. Nilsson, J. Pallon, A. Shariff
Nucl. Instr. and Meth. B 231 (2005) 524-529.

I designed and implemented a new setup for hydrogen analysis at the sub-micron beamline, planned and carried out the experiments. I expanded the data analysis to allow depth profiling for a broad angle interval and wrote the paper.

Paper III **Development of a microtomography system at the Lund sub-micron beamline**

M. Wegdén, M. Elfman, P. Kristiansson, N. Arteaga Marrero,
V. Auzelyte, K.G. Malmqvist, C. Nilsson, J. Pallon
Nucl. Instr. and Meth. B 249 (2006) 756-759.

I designed and implemented a system for microtomography at the sub-micron beamline. I performed simulations and developed a computer code for image reconstruction. I planned and carried out the experiment, took care of the sample preparation, data reconstruction and image visualisation. I wrote the paper.

Paper IV **A feasibility study on the use of focused ion beams for porosity characterisation in bentonite clay**

Marie Wegdén, Per Kristiansson, Daniel Svensson, Anders Sjöland,
Natalia Arteaga-Marrero, Mikael Elfman, Klas Malmqvist,

Charlotta Nilsson, Christer Nilsson, Jan Pallon
Submitted to Nucl. Instr. and Meth. B

I planned and carried out the experiments and was responsible for all data evaluation, analysis, tomographic reconstruction and image visualisation. I wrote the paper, with some support from co-author Daniel Svensson in the geological background.

Related publications not included in this thesis

Conference abstracts

1. **A pre-target charge measurement system for "pixel-by-pixel" normalisation**
   M. Wegdén, M. Elfman, P. Kristiansson, N. Arteaga Marrero, V. Auzelyte, K.G. Malmqvist, C. Nilsson, J. Pallon
   10th International Conference on Nuclear Microprobe Technology and Applications, Singapore 2006

*2. **Micro-analysis of hydrogen in minerals by use of a proton beamline technique**
   H. Skogby, M. Wegdén and P. Kristiansson
   Goldschmidt Geochemistry, Copenhagen 2004

*3. **Hydrogen micro-analysis in minerals by a proton-proton scattering technique**
   H. Skogby, M. Wegdén and P. Kristiansson
   Nordic Geological Winter Meeting, Uppsala 2004 (GFF Vol 126, p 73).

In peer-reviewed international scientific journals

1. **The new Cell Irradiation Facility at the Lund Nuclear Probe**
   N. Arteaga-Marrero, J. Pallon, M.G. Olsson, V. Auzelyte, M. Elfman, P. Kristiansson, K. Malmqvist, C. Nilsson and **M. Wegdén**
   Nucl. Instr. and Meth. B 260 (2007) 91-96.

2. **Symbiotic fungi that are essential for plant nutrient uptake investigated with NMP**
   J. Pallon, H. Wallander, E. Hammer, N. Arteaga Marrero, V. Auzelyte, M. Elfman, P. Kristiansson, C. Nilsson, P.A. Olsson and **M. Wegdén**
   Nucl. Instr. and Meth. B 260 (2007) 149-152.

*   *I contributed by carrying out the experiments and data analysis*

3. **Exposure parameters for MeV proton beam writing on SU-8**
Vaida Auzelyte, Mikael Elfman, Per Kristiansson, Christer Nilsson, Jan Pallon, Natalia Arteaga Marrero and **Marie Wegdén**
Microelectronic Engineering 83 (2006) 2015-2020.

4. **Fabrication of phosphor micro-grids using proton beam lithography**
V. Auzelyte, M. Elfman, P. Kristiansson, J. Pallon, **M. Wegdén**, C. Nilsson, K. Malmqvist, B.L. Doyle, P. Rossi, S.J. Hearne, et al.
Nucl. Instr. and Meth. B 242 (2006) 253-256.

5. **On-line measurement of proton beam current in pA range**
V. Auzelyte, F. Andersson, M. Elfman, P. Kristiansson, J. Pallon, **M. Wegdén**, C. Nilsson and N. Arteaga Marrero
Nucl. Instr. and Meth. B 249 (2006) 760-763.

6. **Evaluation of a pre-cell hit detector for the future single ion hit facility in Lund**
Charlotta Nilsson, Jan Pallon, Göran Thungström, Natalia Arteaga, Vaida Auzelyte, Mikael Elfman, Per Kristiansson, Christer Nilsson and **Marie Wegdén**
Nucl. Instr. and Meth. B 249 (2006) 924-927.

7. **The Lund Nuclear Microprobe sub-micron set-up. Part I: Ion optics calculation**
Asad Shariff, Vaida Auzelyte, Mikael Elfman, Per Kristiansson, Klas Malmqvist, Christer Nilsson, Jan Pallon and **Marie Wegdén**
Nucl. Instr. and Meth. B 231 (2005) 1-6.

8. **The Lund Nuclear Microprobe sub-micron set-up. Part II: Beam line, focusing system and scanning**
A. Shariff, C. Nilsson, V. Auzelyte, M. Elfman, P. Kristiansson, K. Malmqvist, J. Pallon and **M. Wegdén**
Nucl. Instr. and Meth. B 231 (2005) 7-13.

9. **The Lund Nuclear Microprobe sub-micron set-up. Part III: Sample stage, optical imaging and detector configuration in the experimental chamber**
M. Elfman, J. Pallon, V. Auzelyte, P. Kristiansson, K. Malmqvist, C. Nilsson, A. Shariff and **M. Wegdén**
Nucl. Instr. and Meth. B 231 (2005) 14-20.

10. **Optimization of PIXE-sensitivity for detection of Ti in thin human skin sections**
Jan Pallon, Mats Garmer, Vaida Auzelyte, Mikael Elfman, Per Kristiansson, Klas Malmqvist, Christer Nilsson, Asad Shariff and **Marie Wegdén**
Nucl. Instr. and Meth. B 231 (2005) 274-279.

11. **Nuclear microprobe analysis of the selective boron uptake obtained wih BPA in brain tumour tissue**
M. Wegdén, P. Kristiansson, C. Ceberg, P. Munck af Rosenschöld,
V. Auzelyte, M. Elfman, K.G. Malmqvist, C. Nilsson, J. Pallon, A. Shariff
Nucl. Instr. and Meth. B 219-220 (2004) 67-71.

12. **Evaluation of low-energy tailing parameters of a HPGe X-ray detector to be used in GUPIX software library for PIXE analysis**
Asad Shariff, Bengt G. Martinsson, Vaida Auzelyte, Mikael Elfman,
Per Kristiansson, Klas G. Malmqvist, Christer Nilsson, Jan Pallon and
Marie Wegdén
Nucl. Instr. and Meth. B 219-220 (2004) 110-114.

13. **The beam blanking system for microlithography at Lund Nuclear Microprobe**
Vaida Auzelyte, Mikael Elfman, Per Kristiansson, Klas Malmqvist,
Lars Wallman, Christer Nilsson, Jan Pallon, Asad Shariff and **Marie Wegdén**
Nucl. Instr. and Meth. B 219-220 (2004) 485-489.

14. **Characterization of a new large area HPGe X-ray detector for low beam current application**
Asad Shariff, Per Kristiansson, Vaida Auzelyte, Mikael Elfman,
Klas G. Malmqvist, Christer Nilsson, Jan Pallon and **Marie Wegdén**
Nucl. Instr. and Meth. B 219-220 (2004) 494-498.

15. **Development of a system for determination of the ^{13}C/^{12}C isotopic ratio with high spatial resolution**
Per Kristiansson, Tomas Hode, Vaida Auzelyte, Mikael Elfman,
Klas Malmqvist, Christer Nilsson, Jan Pallon, Asad Shariff and **Marie Wegdén**
Nucl. Instr. and Meth. B 219-220 (2004) 561-566.

16. **An off-axis STIM procedure for precise mass determination and imaging**
Jan Pallon, Vaida Auzelyte, Mikael Elfman, Mats Garmer, Per Kristiansson,
Klas Malmqvist, Christer Nilsson, Asad Shariff and **Marie Wegdén**
Nucl. Instr. and Meth. B 219-220 (2004) 988-993.

Contents

Introduction

Focused ion beams can be employed as probes for the examination of chemical and structural features in a sample. Scattered ions or reaction products from the ion interaction with nuclei or electrons in the material can be detected and provide this information. Because of the limited range of ions in matter, the standard ion beam techniques offer only near-surface information, unless the samples are sectioned to a few tens of micrometers and are analysed in transmission geometry.

In STIM (scanning transmission ion microscopy) analysis the energy loss of the transmitted ions serves as a measure of the electron density in the material, i.e. the mass density. This parameter can be mapped in two-dimensional images. These images suffer from the same limitations as X-ray images in medicine. The depth information is lost and there is an overlap of structures in the image, which makes correct interpretation impossible or very difficult. This can be remedied by a tomographic examination of the sample, where the three-dimensional information is reconstructed from a large series of projection data by which the sample is "viewed" from many different angles.

Another method to achieve depth information, in this case on the distribution of a specific element in the sample, is by the elastic scattering technique. The measurement can be made element-specific if the scattering kinetics is fully taken advantage of, in terms of detector positioning as well as timing information. Such a technique is suitable, for instance, for the study of diffusion profiles with high depth resolution.

This thesis is based on the work presented in papers I-IV. They describe different ion beam techniques that I have applied to answer questions in geological applications that require depth profiling or three-dimensional information. Emphasis is given to the development of the analytical method, implementation of the experimental setup and data analysis. All the experimental work has been performed at the Lund Nuclear Microprobe, which is an instrument for complex element analysis.

Paper I and II involve work on hydrogen determination in nominally anhydrous minerals. The low concentrations of hydrogen in these minerals require a very sensitive, hydrogen-specific analytical technique. The technique must be able to distinguish bulk hydrogen from surface contaminations. These requirements are fulfilled with the elastic proton-proton scattering technique, which both gives concentration and depth information with high precision.

In paper III, the development and implementation of a system for STIM tomography is described together with results on test samples. Paper IV describes how the STIM tomography technique is utilised for studies of the porosity in the clay material bentonite. Here also multi-element mapping using the PIXE (particle-induced X-ray emission) technique is performed, in order to obtain complementary information, as well as hydrogen analysis to measure the water content in the clay.

The thesis is divided into four main chapters. My intention is to give a more detailed description of the analytical methods, their implementation and some applications, than what is possible in the restricted space of the papers. Chapter 2 begins with a short introduction to common analytical techniques, followed by a description of the Lund Nuclear Microprobe facility. In chapter 3, the p-p scattering technique for hydrogen analysis is described in detail and chapter 4 deals with microtomography, starting out with a theoretical background, followed by a description of the Lund system and some experimental results.

Ion beam techniques at a nuclear microprobe

An ion can undergo a number of processes when it interacts with matter, for example, elastic and inelastic scattering with the nucleus or electrons in the material. It can also induce radiation by interacting with bound electrons or cause emission of secondary electrons or ions. Ion beam analysis is performed by detecting the energy distribution of the emitted particles or radiation, either of which can be useful in characterizing a specimen and can provide information about elements, isotopes or chemistry. Ion beam analysis refers to several analytical techniques, among others, PIXE, RBS, ERDA and NRA [1].

Nuclear reaction products

γ – rays

Ion beam

X-rays

Backscattered particles

Secondary electrons

Light

Recoil nuclei

Transmitted particles

Forward scattered particles

TARGET
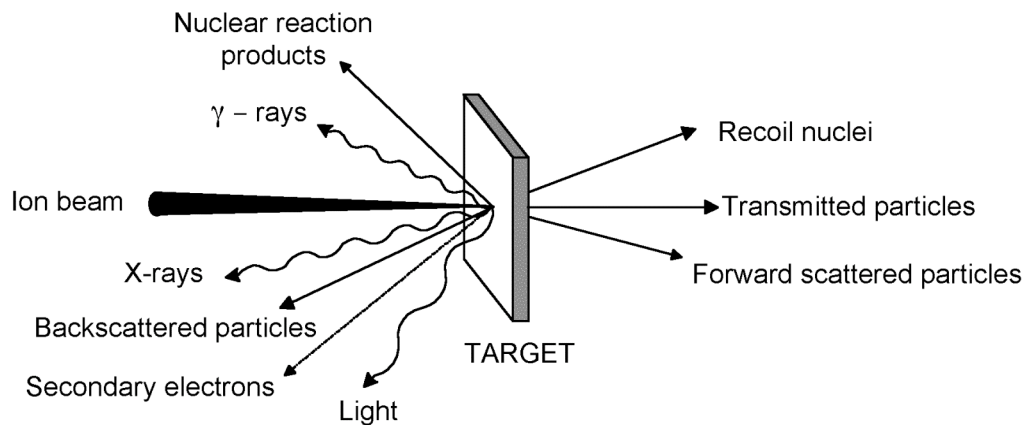
Figure 2.1. *Various processes that can occur when an MeV ion beam interacts with matter.*

A focused ion beam from an accelerator can be used to extract information of microscopic scale from a sample. Combined with other instrumentation (detectors, data acquisition system etc.) it can be used as a micro analytical tool: a *nuclear microprobe* (NMP). The instrument can be used to determine concentrations of elements with high sensitivity. Coupled with a scanning system, two-dimensional "depth-average" distribution information can be generated with a lateral resolution of a few micrometers or less.

The benefit of ions at MeV energies, e.g. in comparison with electrons, is that they penetrate deeply (a few tens of micrometers) without marked scattering, and consequently retain the beam spot resolution to a significant depth [2]. Most of the individual particles penetrate the specimen and roughly retain their incident direction. Only a small proportion of the particles will come sufficiently close to the nucleus of an atom in the specimen to scatter or cause nuclear reactions and be lost from the beam.

2.1 Analytical techniques

The analytical techniques available for a nuclear microprobe can be divided into two classes: high beam-current techniques and low beam-current/single ion techniques. The low beam-current techniques, e.g. STIM, can generate images with better spatial resolution, but the high-beam current techniques (e.g. PIXE, NRA, RBS and ERDA) are better for analytical purposes. Among the analytical techniques described here, the largest cross sections are attained for PIXE, followed by RBS and ERDA. NRA normally has significantly smaller cross sections.

2.1.1 Particle-induced X-ray emission (PIXE)

Particle-induced X-ray emission is based on the excitation of electrons from the inner shells of the atom, induced by a colliding charged particle, e.g. protons or alpha particles. Outer shell electrons recombine with the vacancy, and result in X-ray emission at an energy characteristic of the atom under bombardment. PIXE is a multi-element method (see figure 2.2) with a practical use for all elements heavier than manganese or aluminium. Characteristic X-ray energies for elements with lower atomic numbers (<Al) are so small that they are absorbed in the detector window [3], but to cover also elements in the lower part of the periodic table, PIXE is often supplemented by other techniques that can provide complementary information on the specimen.
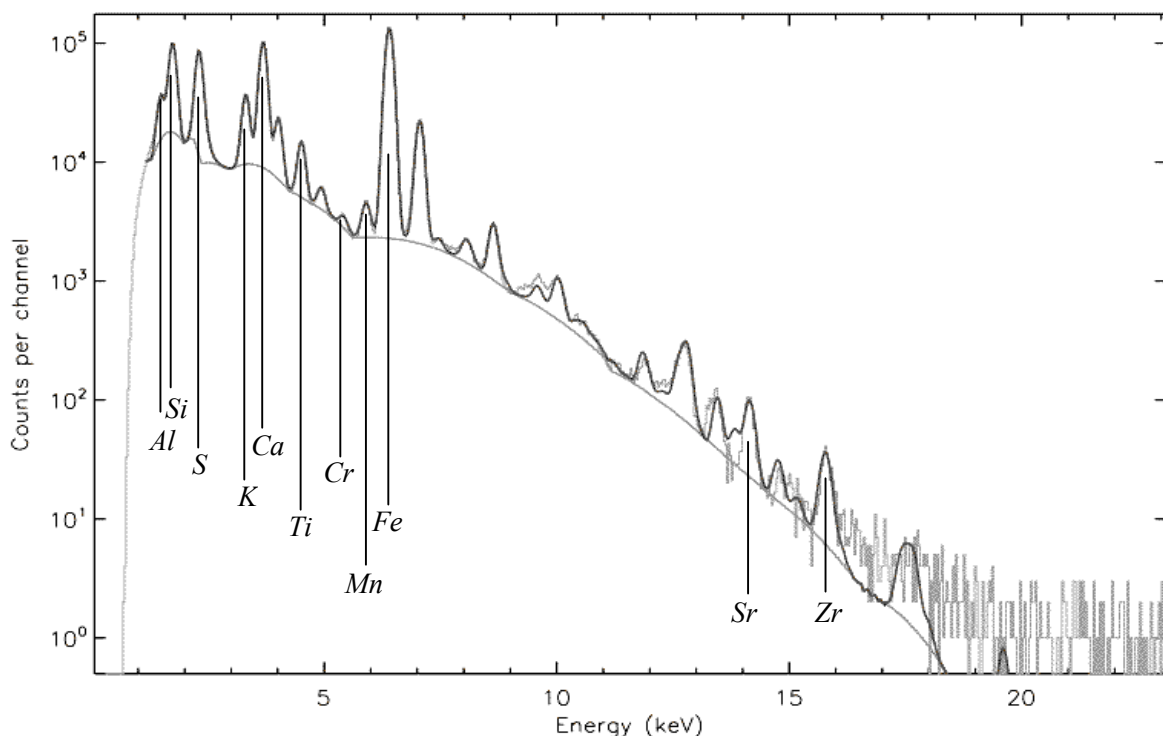
Figure 2.2. *Typical multi-element PIXE spectrum from an aerosol sample. Some peaks are marked with their corresponding element, in order to illustrate the principle for element identification.*

PIXE analysis is fast, essentially non-destructive and the low background facilitates trace element analysis in small samples. With a spatial resolution of a few micrometres, absolute detection limits of the order of $10^{-15} - 10^{-16}$ g can be obtained for thin samples [4]. The detection limit, however, depends on several factors, such as the target element, the sample matrix and the energy of the projectile. Therefore the detection limit has to be separately evaluated for every sample and element.

2.1.2 Nuclear reaction analysis (NRA)

Highly energetic particles can penetrate the Coulomb barrier of an atomic nucleus, and a nuclear reaction, leading to the formation of reaction products such as protons, alpha particles, neutrons or gamma rays, will occur. This can be written as:

$$a + X \rightarrow Y(*) + b + Q$$
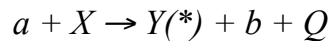
or in shorter form as $X(a,b)Y$. The accelerated projectile, a, collides with the target nucleus X and creates the reaction products Y and b. Q is the energy created by the process. b is often used for analysis since it is the lightest of the products, but as Y often ends up in an excited state its deexcitation photons can also be detected.

The height of the Coulomb barrier that must be overcome is

$$E_C = \frac{Z_1 Z_2 e^2}{4\pi\varepsilon_0(R_1 + R_2)} \approx \frac{Z_1 Z_2}{(A_1 + A_2)^{1/3}} \left[MeV \right] \tag{2.1}$$

where the impinging particle has charge $Z_1 e$ and radius R_1, and the target nucleus has charge $Z_2 e$ and radius R_2. In general the lightest particles (p, d, ^{3}He etc.) with an energy of a few MeV are used for target atoms with Z<20.

The cross sections are largest when light ions interact with light nuclei (Z<20), although quantum mechanical tunnelling provides a small probability to penetrate higher barriers. However, the cross sections, and consequently also the count rates, are generally low. For this reason, large solid angle detectors are a necessity and high beam-currents and/or long collection times are required for good statistics. Nuclear reaction analysis relies on the measurement of the energy of the reaction products in order to identify the target nucleus, but different target elements can produce identical reaction products at similar energies. In addition, more than one reaction can be possible for a certain nucleus, which results in an overlap between different reaction products (or the same reaction product at different energies if the target nucleus has a number of excited states close to the ground state) [5]. This complicates the identification of the target nucleus, and therefore the usual mode of operation is to match the energy of the projectile to a specific, known nuclear resonance in the target nucleus [4] or use an appropriate filtering technique, e.g. an absorber, time-of-flight measurement or coincidence technique [5].

Depth profiling is performed by step-by-step energy advancement of the specific nuclear reaction resonance in the bulk. With narrow resonances, this can be achieved with nanometre resolution.

Particle-induced gamma-ray emission (PIGE) is a form of NRA where the detected reaction product is a gamma ray. The method can be useful for detecting some elements, but with limited sensitivity because of the generally low cross sections, as in NRA. Depth information is normally not achieved, with the exception of resonance reactions.

2.1.3 Rutherford backscattering spectrometry (RBS)

When the energy of the projectile is much smaller than what is required to overcome the Coulomb barrier, the primary mechanism is elastic scattering between the projectile and the target nucleus [3]. The scattering process is caused by the Coulomb repulsion between the two charges and obeys simple classical laws, with conservation of energy and momentum. A light particle that collides with a heavier target nucleus, will scatter in the backward direction and transfer an amount of energy corresponding to $E_0(1-K)$, where K is the kinematic factor defined as

$$K = \frac{E_1}{E_0} = \left(\frac{M_1 \cos\theta + (M_2^2 - M_1^2 \sin^2\theta)^{1/2}}{M_1 + M_2} \right)^2 \qquad (2.2)$$

where E_0 and E_1 are the energies of the incident and the scattered particle, respectively. M_1 is the mass of the incident particle, M_2 of the target nucleus and θ is the scattering angle in the laboratory system. Also the differential scattering cross section is written as

$$\left(\frac{d\sigma}{d\Omega} \right)_{lab} = 1.296 \left(\frac{Z_1 Z_2}{E_0} \right)^2 \left[\sin^{-4}\left(\frac{\theta}{2} \right) - 2\left(\frac{M_1}{M_2} \right) + ... \right] \qquad (2.3)$$

where Z_1 and Z_2 are the charges of the incident ion and of the scattering nucleus.

The method is better for heavier elements as the cross section depends on Z^2, and typically about 100 µg/g of a heavy element can be quantified in a light matrix [1]. Differential cross sections of alpha particles at backward angles can be in the 1-10 b/sr range for middle-Z elements, which is smaller than for PIXE. For the light elements (Z<12) the differential cross sections at backward angles are in the 1-100 mb/sr range and are in general smaller than the equivalent specific nuclear reaction cross sections [3].

The energy of the backscattered ion is measured at a well-defined angle (usually as close to 180° as possible to improve the mass resolution) in order to determine the mass of the scattering nuclei, and with a knowledge of the reaction cross section also the stoichiometry of the sample. The energy loss of ions due to electron collisions is well-defined, and thus also the depth of the scattering nucleus can be determined to produce depth profiles of elements, typically with a depth resolution of a few tens of nanometres [1,4]. The major advantage of RBS over NRA and PIXE is that depth profiling can be carried out in a fast, simple and direct manner [3].

2.1.4 Elastic recoil detection analysis (ERDA)

ERDA is related to RBS, but here the energy of the recoiling target nucleus is measured. The kinematics allows the recoil to occur only in the forward hemisphere

and the projectile, which is often incident at a glancing angle, should have a higher mass than the target nucleus. ERDA complements RBS in measuring light elements in matrices of medium or high average atomic number. An absorber foil in front of the detector stops scattered beam particles and allows only ejected particles to reach the detector, at the price of degrading the depth resolution. High-resolution ERD systems with electrostatic deflectors for blocking scattered beam particles overcome this problem, and depth resolutions of 0.28 nm have been reported [6].

2.1.5 Scanning transmission ion microscopy (STIM)

The method is based on the measurement of the energy loss of beam particles travelling through the sample. The energy loss is caused by ion-electron interactions and the magnitude of the total energy loss depends on the elemental concentration, mass density and thickness of the sample.

On-axis STIM provides high spectral resolution, and requires the detection of only a few transmitted particles. This is advantageous for samples that are sensitive to mass loss when higher beam intensities are used. Another option is to position the detector at some suitable angle, a setup called off-axis STIM. Since the angle between the beam and the detector is small (10–15°) the information is about the same as with on-axis STIM. Off-axis geometry makes it possible to use analytical beam-currents and STIM analysis can thus be performed simultaneously with for example PIXE or RBS, but spectral degradation will decrease the contrast compared to the on-axis case. The particles can also reach the detector by scattering in a thin carbon foil placed behind the sample (on-axis/off-axis STIM). The geometry is then sensitive only to pure energy loss, and ions scattered in the sample will not influence the spectral shape because they are off-collimated [7]. Figure 2.3 shows a STIM map of fungi spores with visible internal structures.
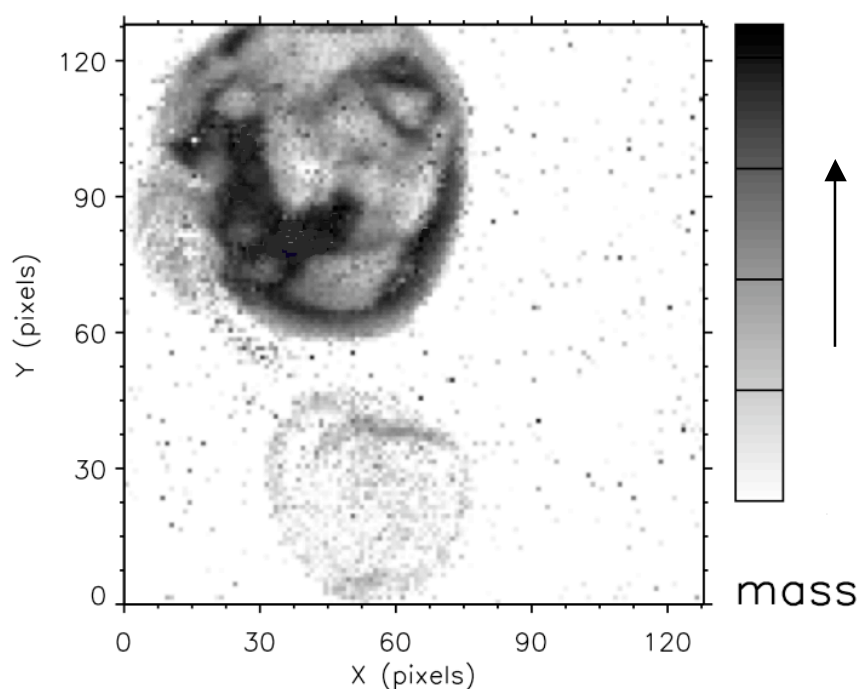
Figure 2.3. *STIM map of fungi spores. Notice the internal structure in the upper spore. Pixel size: 1 μm.*

2.1.6 Secondary electron imaging (SEI)

Bombarding ions cause secondary electrons to be sputtered from the surface atoms. If these low energy electrons are collected at a shallow angle, they can provide information on the surface structure of the sample and be used for imaging light elements. For heavy elements the contrast is too poor.

2.1.7 Ion beam induced luminescence (IBIL)

Ionoluminescence is an atomic phenomenon, which relies on the excitation of electrons in the outer atomic shells by ion collisions. During the deexcitation electromagnetic radiation in the infrared to ultraviolet region is emitted, which gives information on the chemical nature of the atom.

2.2 Ion beam material modification

Ion beams cannot only be used for element analysis but also for material modification due to the damage induced by ions in matter. For example, organic molecules may, when struck by high-energy particles or photons, break down into smaller fragments or cross-link to form larger molecules. An example of this is proton beam lithography (PBL), which has been successfully performed over recent years at the Lund Nuclear Microprobe [8-11].

2.2.1 Proton beam lithography (PBL)

A focused MeV proton beam can be used to produce microstructures. The proton beam is rastered in a controlled way over a sensitive material, a resist, which is modified by the beam. The resist is developed and removed, either where it was hit by the beam (positive) or everywhere else (negative). Due to the long range and small straggling of protons compared to e.g. electrons, structures with a high aspect-ratio can be produced [12]. Another advantage is that there is no need for a mask, like in photon lithography, since the beam can be scanned over the resist in any user-defined pattern with the help of a fast beam blanking system.

2.3 Single ion irradiation

During the past few years, the Lund Microgroup has taken part in the Marie Curie Research Training network "Cellion", which aims at the study of low dose cellular response. The low dose is represented by single ions, which can be isolated from an ion beam and be used for targeted irradiation of cells. The purpose of the irradiation is to study typical cellular response, such as the bystander effect, adaptive response and genomic instability.

The single ions are achieved by shutting both object and aperture slits to a minimum until a very small beam current is reached, and the event of the target being struck by a single ion is confirmed by a signal from a pre-target or post-target detector system. This signal controls a beam deflector, which makes sure that only a pre-set

number of ions hit the target, and deflects the beam off the sample when that criterion is fulfilled. [13-15]

2.4 The Lund Nuclear Microprobe laboratory

The Lund Nuclear Microprobe laboratory is based around a single-ended electrostatic 3 MV Pelletron accelerator (model NEC 3 UDH). Inside the pressure tank is a radio-frequency ion source, which can produce protons, alpha particles and occasionally also deuterons from hydrogen, helium and deuterium gas. The pressure tank is filled with insulating gas, SF_6, to prevent sparking. The ions that are produced in the ion source are pre-focused by the Einzel lens and the correct ion charge state is selected with the velocity selector.

Charge is inductively sprayed onto the pellet chain and picked off at the high voltage terminal to create a potential difference between the HV terminal and ground at the exit side of the accelerator. The ions from the ion source are then accelerated towards ground, attaining a maximum energy of 3 MeV per unit charge. The accelerated ions experience some further focusing and steering before entering the analysing magnet, which serves as a momentum filter where ions of the correct charge and velocity are selected to pass into one of three beamlines: *macro, micro and sub-micron*, each leading to a separate experimental chamber via a beam optimisation system. Along the beamlines vacuum pumps are strategically positioned to maintain high vacuum along the beamline and in the experiment chamber.

The experimental work described in this thesis has mainly been conducted at the sub-micron beamline, but the early work (paper I) was performed at the micro beamline.

2.4.1 Beam transport and focusing

Magnetic quadrupole lenses are widely used to focus MeV ions. Since a quadrupole magnet focuses in one plane and diverges the particle beam in the other, at least two quadrupoles of opposite polarity are needed to focus an ion beam [3]. The demagnifiacation of the ion beam onto the target is set by a combination of the size of the object collimator, the distance from the object slit package to the target and the properties of the focusing magnets. The shaping and elimination of divergent parts of the beam are performed with the aperture slits. Different combinations of object and aperture slit size, together with the excitation of the quadrupole magnets, control the beam size and current conditions. Along the beamlines there are several devices responsible for facilitating the transport and focusing of the beam, e.g. electrostatic and magnetic steerers and beam profile monitors. Beam stops and viewers assist in the optimisation of the beam. The three beamlines are schematically shown in figure 2.4.

2.4.2 Beamlines and experiment chambers

The first beamline, the macro beamline, is situated at +30° from the exit port of the accelerator and utilizes a quadrupole doublet to produce an enlarged homogeneous beam (1-10 mm) in the chamber, with a typical current between 1 and 200 nA [16,17].

This beamline is used mainly for quantitative PIXE analysis of for example aerosol samples.

The second beamline, the micro beamline, is situated at +15° and utilizes a quadrupole triplet for beam focusing, typically producing a beam spot of 1-10 μm with currents of 100-1000 pA.
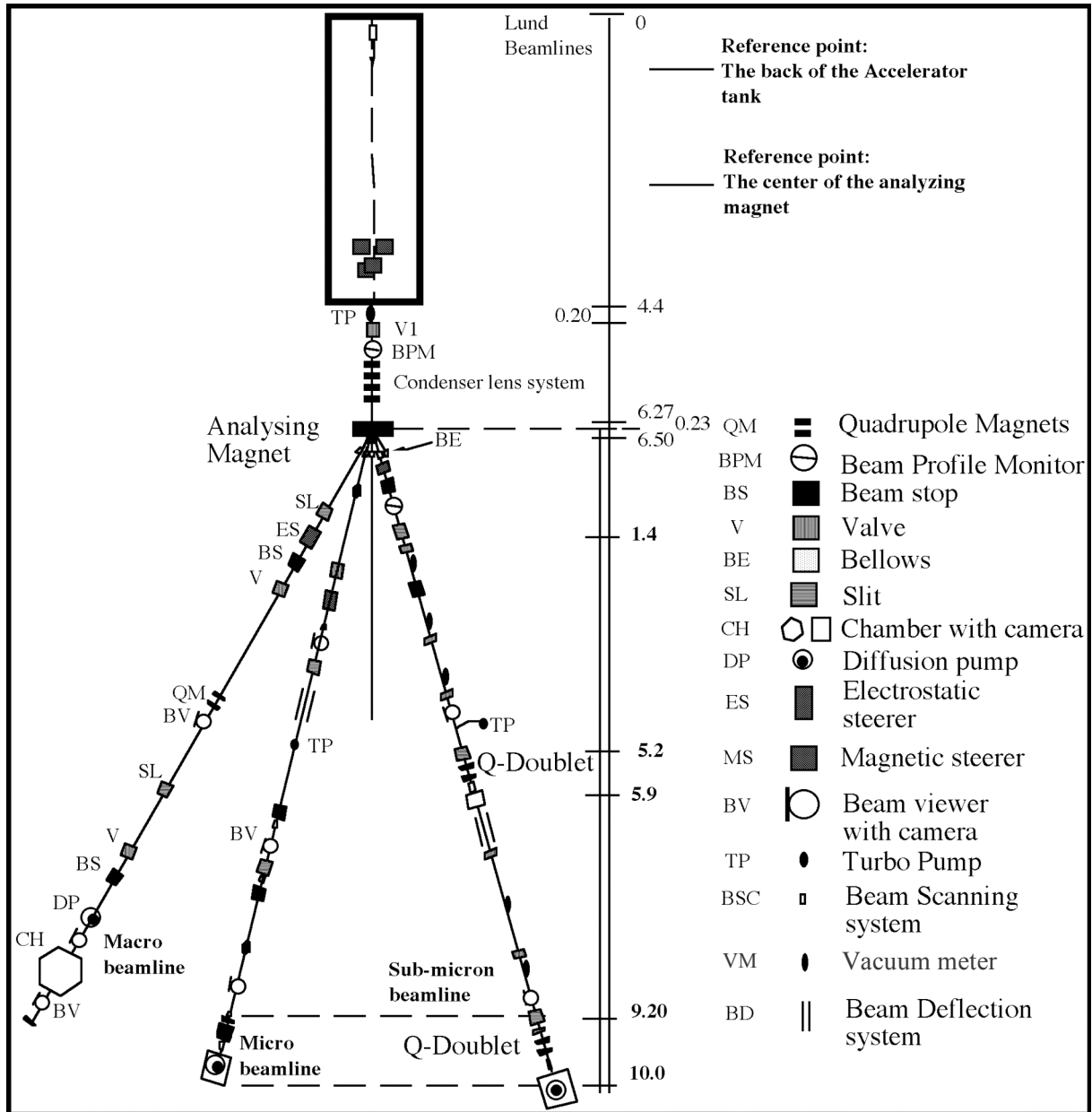
Figure 2.4. *Schematic diagram of the three beamlines at the Lund Nuclear Microprobe*

The third and most recently installed beamline is the sub-micron beamline, situated at -15°. It has a two-stage focusing system consisting of two separated doublets, where the beam is focused to a small spot in the first stage, which is then used as object in the second stage in which the ion beam is demagnified again to sub-micrometre dimensions [16]. Theoretical calculations on beam optics show that a beam spot of 200 nm × 500 nm is attainable with this setup [18]. The beamline was mechanically ready

late in 2003 and since then the work on further development, installations in the experiment chamber, as well as testing and optimisation of the beam optics has continued.

Since a reduction of the beam spot is made at the expense of beam current, an annular, large-area HPGe-detector (8 × 100 mm^2) has been installed for traditional PIXE analysis [19]. The large and flexible experiment chamber can accomodate other detectors, such as surface barrier detectors in the forward or backward direction for NRA, RBS or other scattering experiments. Small detectors can easily be mounted on the movable stage for chamber microscope objectives. The chamber is equipped with a movable X-Y-Z sample stage controlled by step motors with nm precision. For tomography experiments, the sample holder can be replaced by a rotation motor (DC-Motor-Gearhead C136-10 drive unit), which is capable of high precision rotation in steps of 0.0068° at an approximate speed of 1200°/s.

The micro and sub-micron beamlines are equipped with post-lens magnetic scanning systems, which are used for rastering the beam over a large sample area to obtain two-dimensional information on the elements in the sample. The in-chamber configuration of the scanning system at the sub-micron beamline was chosen on the basis of the short design distance between the last quadrupole doublet and the chamber. This configuration restricts the scanning area to a maximum of approximately 3 mm × 3 mm. Scanning frequencies of 1 kHz are possible with good accuracy for the beam positioning, with an option of 10 kHz for small scanning sizes.

2.4.3 Fast beam blanking and charge measurement

Both the micro and the sub-micron beamline have fast beam blanking systems, for instance for proton beam lithography experiments, when the beam needs to be blanked during movement between pattern pixels or to control beam exposure times. The electrostatic blanker plates are controlled by a TTL signal that is fed to a high voltage amplifier and the beam is deflected off the sample within 200 ns [9].

All three experiment chambers allow charge measurement in Faraday cups in transmission geometry or from the sample via the sample holder. An important improvement at the sub-micron beamline is that the beam blanker is combined with a pre-target Faraday cup for accurate and sample-independent charge measurement [20]. The beam is blanked into the pre-target Faraday cup at some point during the exposure of the sample. How often, and for how long the charge is measured depends on how much beam time the experimentalist is prepared to sacrifice. Typically it is reasonable to sacrifice 10-20% of beam time in high-precision charge measurements. If only the total charge is needed for charge normalisation, the beam can be deflected more seldom, but for pixel-by-pixel normalisation, the beam must be deflected at the same rate as the scanning frequency.

The readout of the Faraday cup is made either by connecting it to a charge integrator or to a Keithley 6514, low-current electrometer. The charge integrator has a sensitivity level of 100 pulses / pC, but has a recovery time of 0.5 s, which makes pixel-by-pixel charge or current measurement impossible at standard scanning frequencies. The Keithley electrometer can measure currents in the fA region, but with long integration times (typically 2.5 s). Therefore this instrument is useful only for

measurements for low beam-current control and adjustment, not for charge or current measurements under data acquisition conditions.

The pre-target Faraday cup could be replaced by a sensitive particle detector for low current measurements, but then cannot be used for any of the applications that require normal current conditions for analysis. With the pre-target Faraday cup, the flexibility of the charge measurement system is maintained, and it can be used for a wide range of beam current conditions.
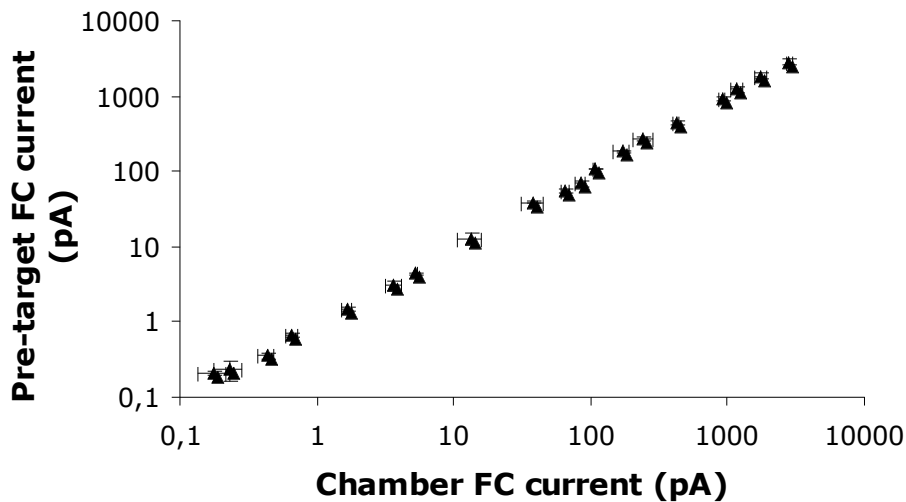
Figure 2.5. *Charge measured in the chamber Faraday cup (FC) and the pre-target FC with the Keithley 6514 Electrometer, showing good linearity over the whole current range.*

2.4.4 NIM electronics and data acquisition system

Most experiments require the use of pulse electronics such as spectroscopy amplifiers, timing units and discriminators for signal handling. These modules follow the *NIM (Nuclear Instrumentation Module)* standard, which was defined for experiments in nuclear and particle physics in the 1960s. The standardisation involves module dimensions and electrical specifications, and the modules fit into standardised power bins for voltage supply. The NIM logic signals are categorised into slow-positive and fast-negative types.

The data acquisition system takes care of the final beam control, such as pattern scanning, takes care of coordinate tagging of every event and handles the data flow from detectors and charge measurement systems. The Lund CAMAC based data acquisition system is fast and can process high count rate data with low dead time. It is capable of acquiring data in event-by-event mode, read 8 ADC channels in parallel and store and display the data. [21,22]

Hydrogen analysis with ppm-sensitivity

Hydrogen is the most abundant element in the cosmos, and is one of the main constituents in water and organic material. It is also the most common elemental contaminant and its presence can have dramatic effects on the electrical, mechanical and chemical properties of materials. Having a valence of both +1 and -1, it is chemically versatile and can react with most elements. Hydrogen is also by many orders more mobile than other common contaminants, even at room temperature. [3]

Many research disciplines such as geology, materials science, biology and medicine have a strong interest in quantitative and spatially resolved data on the hydrogen distribution in a sample. Examples are hydrogen quantification and depth profiling in minerals to understand mechanisms for conductivity, water storage capability and circulation in the mantle of the Earth or examination of CVD-grown diamond to localise the position of hydrogen defects [23-27].

Every application has its own special needs, either concerning radiation-sensitive samples, low hydrogen concentrations, demands on resolution etc., and the analytical method to provide answers to the specific questions, must be adapted to fit the special requirements. Hydrogen is also considered to be one of the most difficult elements to analyse [6]. Most common analytical techniques, such as PIXE, RBS, Auger electron spectroscopy etc. cannot detect hydrogen. Variations on ERDA and NRA are widely used, but are considered to be restricted to surface analysis or require projectile species and/or energies, which are not available at the Lund Nuclear Microprobe facility.

In this thesis work, I have concentrated on developing the p-p scattering method, first proposed by Cohen et al. in 1972 [28], for straight-forward analysis of mineral samples with low hydrogen content. The reduction of the background due to random noise and the influence of other elements, to achieve a sensitive and background-free measurement of hydrogen concentrations at the ppm-level, has been given special emphasis. By producing depth profiles, bulk data can be extracted and distinguished from disturbing surface contamination.

3.1 Elastic proton-proton scattering

Proton-proton scattering was introduced by Cohen et al. in 1972. A 17 MeV macroscopic proton beam was used to measure, non-destructively, the depth distribution of hydrogen in thin (2-5 mil) films, also including the identification of surface contaminations of some 100 Å thickness. Coincident detection of scattered and recoiled particles at 45° was carried out to achieve mass selectivity, reduce the background and improve the detection limit to about 1 atomic ppm [28].

The technique requires transmission geometry (see figure 3.1) and that both the recoiled and the scattered particle are detected. Therefore only thin samples can be analysed. Elastic proton-proton (p-p) scattering deals with equal masses of projectile and target nucleus, which at non-relativistic energies has the result in that the sum of the scattering and recoil angles is exactly 90° in the laboratory system. Scattering on hydrogen nuclei (i.e. protons) can therefore be distinguished with high precision from scattering on other elements in the sample. In elastic scattering, both the kinetic energy and the momentum are conserved, and the following equations can be formed:
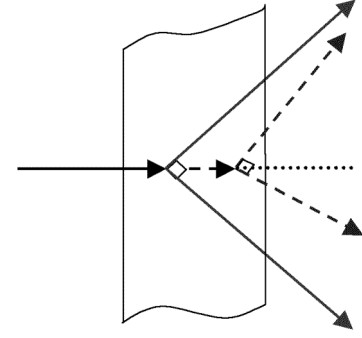
Figure 3.1. *Illustration of the p-p scattering geometry.*
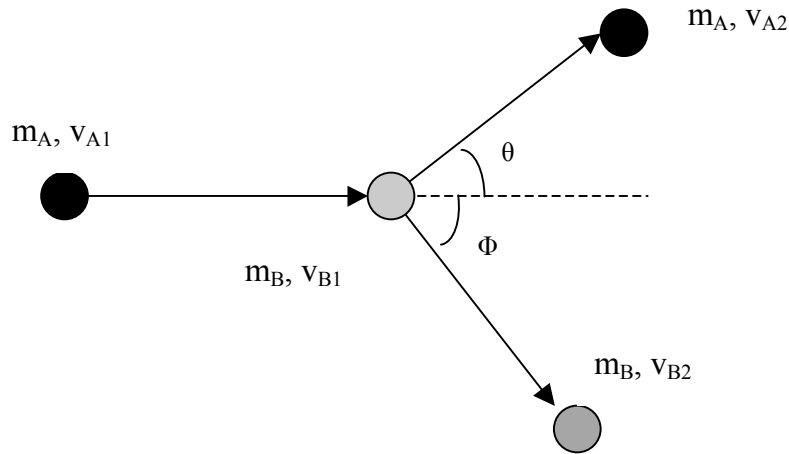
Figure 3.2. *Forward elastic scattering characteristics. θ symbolises the scattering angle, and Φ the recoil angle. The target with mass m_B is assumed to be at rest before the scattering event.*

Kinetic energy:
$$\frac{1}{2} m_A v_{A1}^{2} = \frac{1}{2} m_A v_{A2}^{2} + \frac{1}{2} m_B v_{B2}^{2} \qquad (3.1)$$

Momentum in the x-direction:
$$m_A v_{A1} = m_A v_{A2} \cos\theta + m_B v_{B2} \cos\phi \qquad (3.2)$$

Momentum in the y-direction:
$$m_A v_{A2} \sin\theta = m_B v_{B2} \sin\phi \qquad (3.3)$$

Particle *B* (see figure 3.2) is considered to be at rest before the collision, and after the collision, the scattered and the recoiled particle cannot be distinguished from each other. From this set of equations, an expression for the scattering angle, *θ*, can be derived:

$$\tan\theta = \frac{\sin(2\phi)}{\dfrac{m_A}{m_B} - \cos(2\phi)} = \left\{ if\ m_A = m_B \right\} = \frac{\sin(2\phi)}{1 - \cos(2\phi)} = \frac{1}{\tan\phi} \qquad (3.4)$$

The left-hand side of the equation, subtracted by the right-hand side becomes:

$$\tan\theta - \frac{1}{\tan\phi} = \frac{\sin\theta}{\cos\theta} - \frac{\cos\phi}{\sin\phi} = \frac{-\cos(\theta+\phi)}{\cos\theta\,\sin\phi} = 0 \qquad (3.5)$$

$$\cos(\theta+\phi) = 0 \qquad \rightarrow \qquad \theta + \phi = 90° \qquad (3.6)$$

The sum of the scattering and recoil angles can only be 90° for equal masses of projectile and recoiled particle, and hence if the detectors are positioned wisely, effective mass discrimination can be achieved by the measurements. One alternative is to position two detectors in 45° to the direction of the incident beam, as described by Cohen et al. in their revolutionary paper. However, the detectors must be small, in order not to accept too large an angle interval around 45°. This is not good in combination with the wish for a large solid angle to reduce the radiation damage to the sample. The use of larger detectors, by which the transmitted particles are detected in coincidence, in combination with a scattering and recoil angle identification process, is then a more attractive alternative. Both methods are capable of depth profiling if the residual energy is measured. The major advantage of the latter method lies in the possibility to use large solid angle detectors without sacrificing depth resolution. Another advantage is that the exact positioning of the detectors is not so crucial, which makes the setting up of the experiment less difficult.

Figure 3.3 shows, the angle coverage that would be desirable, in order to avoid signals from disturbing elements, and at the same time maintain an acceptable solid angle. Calculations of recoil angles for elastic scattering on different elements with a proton beam as projectile and scattering angles in the forward hemisphere, show that, with the strict constraint of 90° between scattered and recoiled particle, there is no possibility for simultaneous detection for any other target than hydrogen in the 30-60° interval. This angle interval is chosen symmetrically around 45° with the intention to maximise the solid angle and avoid all interference due to elastic scattering with
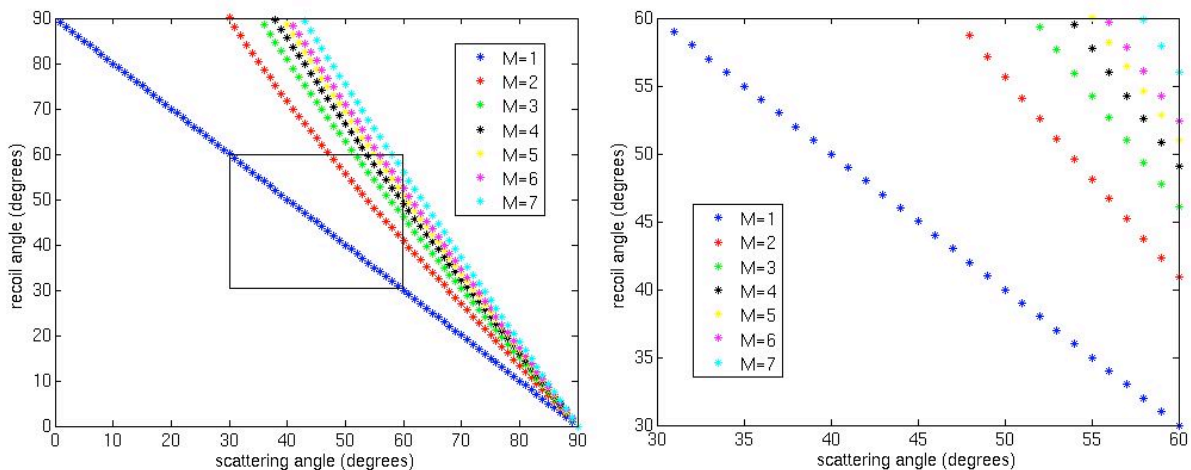
Figure 3.3. *The resulting recoil angle for a target of mass number M when bombarded with protons (M=1) scattered into the forward hemisphere. Figure (b) is a close-up of the boxed region in figure (a) and corresponds to the angle coverage of the hydrogen detector used in the experiments.*

other elements. No overlapping angles whatsoever can be observed in this safe region, and restricting the angle interval even further makes accidental detection caused by multiple scattering impossible. Figure 3.3 also shows that interference is more likely with low-mass elements, which are not common constituents in these samples. Thus major matrix elements cannot contribute to any serious interference with this detector setup. Transmitted particles do not constitute a problem because of their nearly linear propagation in matter. It is not very likely that multiple scattering causes a deviation of the proton direction by as much as 30° and, in combination with a strict coincidence condition, such events are efficiently eliminated. The coincidence condition also deals with inelastic scattering events and particles from nuclear reactions with energies lower than the incident particle. The "one-element specificity" eliminates the problem of background subtraction, which enhances the sensitivity [29].

Over the years, the p-p scattering method has not been widely used as an analytical technique. The method is less conventional than the standard ERDA technique, which does not offer as good damage number (see equation 3.7 for definition) or analytical depth as the p-p scattering method, but, on the other hand, it does not require the same sample preparation technique where the samples are thinned down to allow particle transmission. More recently however, the possibility of using the p-p scattering method in microprobe applications has attracted interest, and is now being applied at microprobe laboratories in Sweden, Germany, France and Japan, both at low and high energies [24,25,30,31]. In Lund, proton-proton scattering experiments have been performed in several application areas. Apart from those described in this work, some examples are: sensitive hydrogen analysis in aerosol samples [32] and design of a detector for thin samples at a nuclear microprobe [33]. Neither of these papers include depth profile measurements.

3.2 Practical aspects and restrictions in hydrogen analysis

Every ion beam analytical method relies on the principle of sending in a projectile, letting it interact with the material and then studying the result of the interaction, for example, in the form of emitted or scattered particles, in order to identify the target nucleus.

In the choice of analytical method, several considerations have to be taken into account. Firstly, the reaction cross section, i.e. the probability of inducing a reaction with the element of interest, should be as high as possible. This can be achieved by tuning the energy of the projectile or in the selection of projectile species. On the other hand, ion beam irradiation always contributes to radiation damage in the sample, which should be kept at a minimum in order not to alter the element distribution in the sample being examined.

Hydrogen analysis in nominally anhydrous minerals, as will be thoroughly described in a later section, makes the following requirements:
  • High sensitivity due to the low hydrogen concentrations
  • Minimum beam damage effect
  • Depth profiling with micrometre resolution

These basic requirements are discussed in the following paragraphs, and the potential of some ion beam analytical techniques, namely, ERDA, NRA and elastic p-p scattering is evaluated. The use of MeV ion beams for hydrogen concentration profiling has been extensively reviewed by Lanford [34]. Also Ziegler et al. [29] present basic approaches on the same topic.

3.2.1 Sensitivity

High sensitivity can be attained for a reaction with a large cross section combined with a large solid angle detector. For good statistics within a reasonable beam time, there is also need for a high count rate, which can be achieved with a high beam current. The beam current is limited by the beam spot size, thus sometimes requiring a trade-off between yield and lateral resolution. Also, there is a need for a balance between fast measurement and the sensitivity of the analysis, because scattering on matrix atoms causes high count rates and therefore a background of accidental coincidences.

An important advantage of p-p scattering compared to other ion beam analytical methods with heavy projectile ions, lies in the increase in the cross section at energies where Rutherford formulas are not applicable (e.g. when the projectile ion has enough energy to penetrate the Coulomb barrier) and the strong interaction contributes considerably to the scattering potential. The limit for Rutherford behaviour for projectiles of different atomic numbers is illustrated in figure 3.4.
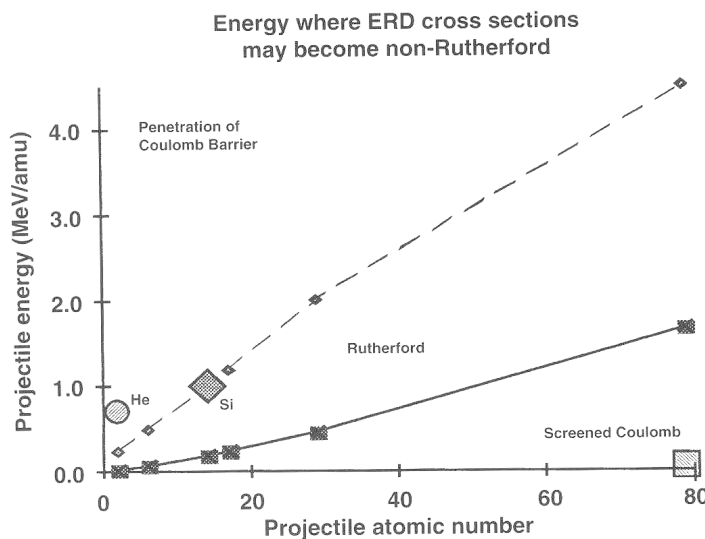
Figure 3.4. *Energies at which the ERD cross section shows non-Rutherford behaviour. Above the dashed line the projectile may have sufficient energy to penetrate the Coulomb barrier and cause non-Rutherford cross sections. Below the solid line, the projectile energy is so low that significant screening of the nuclear charge occurs. From ref [3].*
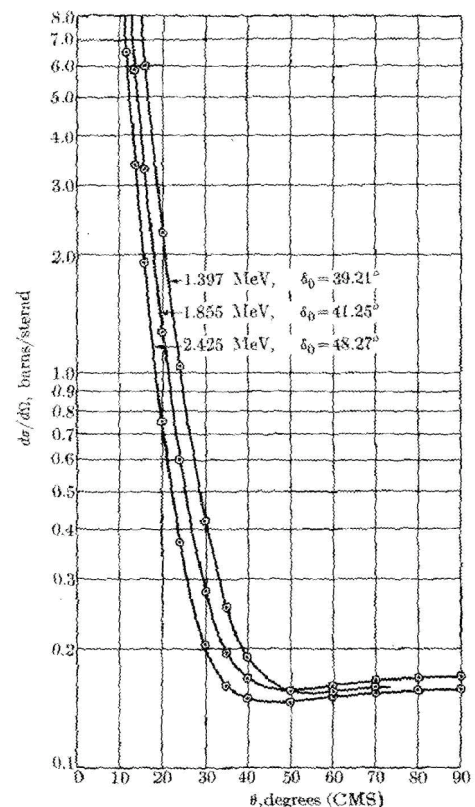
Figure 3.5. *Theoretical and experimental p-p cross sections in the centre-of-mass frame at three energies. From ref [35,36].*

At energies around 2.5-3 MeV the cross section for p-p scattering (figure 3.5) is enhanced by a factor of 50-100 over the scattering cross section expected from a pure Coulomb potential, which is the main strength of the method. Differential cross sections for the candidate techniques are presented in table 3.1.

Table 3.1. *Differential cross sections for candidate techniques and widths of nuclear resonances. From ref [24,34,36].*

Reaction	$d\sigma/d\Omega$ (mb/sr)	Γ (keV)
p-p scattering (2.45 MeV, 45°)	400	–
He-ERD (10 MeV)	800	–
NRA (^{15}N, 6.385 MeV)	131	1.8
NRA (^{15}N, 13.35 MeV)	84	25.4
NRA (^{19}F, 6.418 MeV)	7	44
NRA (^{19}F, 16.44 MeV)	35	86
NRA (^{7}Li, 3.07 MeV)	0.38	81

3.2.2 Radiation damage

All irradiation contributes to a more or less severe modification of the sample, and in many applications radiation damage produced by the ion beam is a key limitation [3]. Radiation damage processes arise from two different mechanisms of energy transfer:

- *Electron stopping*, where energy is lost to electronic excitation and ionisation processes. This is the dominant effect (more than 99 %) for light MeV ions.
- *Nuclear stopping*, where scattering of the incident ion by the target nucleus results in energy transfer to the whole atom. This is the dominant energy-loss process at low (keV) energy.

In metals and most semi-conductors, electronic excitation and ionisation does not lead to permanent damage effects, but in insulators and other molecular compounds, the electronic stopping power may cause bond breakage and hence permanent chemical and structural changes in the target. This does not necessarily induce errors in the quantification, but if the defect species are mobile (*radiation enhanced diffusion*) or volatile, then significant changes in depth distribution or stoichiometry may result [3, 37].

A sensitive quantitative analysis is impossible when the sample is changed by the irradiation before a statistically significant number of events has been detected. Most of the primary damage in most elements consists of only small changes in the position of the atom, which do not affect the analysis at micrometer resolution. For hydrogen, however, more severe damage has been known to occur, as hydrogen when once activated, often diffuses very fast and in this way can leave its original position. Deposited energy also appears as heat released in the target [37]. For micrometer beam spot size and beam currents of 200 pA, this generates an increase in temperature of only 10 K [38]. For this reason thermal effects are not considered to be a problem.

It is impossible to avoid beam-induced damage in targets, but the effects can be reduced, for instance, by limiting the total energy deposition within the irradiated area. This can be achieved either by lowering the beam current, maximizing the beam spot size or decreasing the beam time. None of these options are however compatible with ppm-sensitivity and micrometre resolution, and therefore a technique, which produces the smallest number of ionisations and dislocations must be chosen.

To compare the effective damage action of different ion beam methods, the *damage number*, *D*, can be determined for a thin target as:

$$D_{ion,disp} = \frac{N_{ion,disp}}{N_{det}} = \frac{\sigma_{ion,disp}}{\left(\dfrac{d\sigma}{d\Omega}\right)_{pp} \Delta\Omega} \qquad (3.7)$$

$N_{ion,disp}$ and N_{det} are the number of ionised, displaced or detected hydrogen atoms respectively, and $\sigma_{ion,disp}$ and σ are the cross sections for displacement, ionisation and detection. $\Delta\Omega$ is the solid angle of the detector. Release, displacement and ionisation cross sections for 2.55 MeV and 3 MeV protons in Mylar are shown in table 3.2 and damage numbers for ERDA, NRA and elastic p-p scattering are presented in table 3.3.

Table 3.2. *Cross sections for damage effects from experimental data. Release, displacement and ionisation cross sections have been calculated with the Kinchin-Pease Model. From ref [38].*

	σ_{rel} **(barn)**	σ_{disp} **(barn)**	σ_{ion} **(barn)**
2.55 MeV p on Mylar	$8\cdot10^4$	$1\cdot10^4$	$3\cdot10^7$
3 MeV p on Mylar	$2\cdot10^5$	$1\cdot10^4$	$3\cdot10^7$

Table 3.3. *Damage numbers for different ion beam analytical techniques. From ref [38]. The values for p-p scattering have been calculated from cross section data in figure 3.5, data in table 3.2 and equation 3.7 for the detector used in the experiments ($\Delta\Omega$ = 1.5 sr).*

	Energy (MeV)	**Experimental conditions**	D_{disp}	D_{ion}
p-p scattering	3	$\Delta\Omega$ = 1.5 sr	$2\cdot10^4$	$5\cdot10^7$
ERD	$1\cdot A_1$	$\Delta\Omega$ = 10 msr	$4\cdot10^8$	$7\cdot10^{11}$
He-ERD	10	$\Delta\Omega$ = 100 msr	$7\cdot10^5$	$1\cdot10^9$
NRA (^{15}N, 6.385 MeV)	7	ε = 35 %	$> 4\cdot10^6$	$> 6\cdot10^9$
NRA (^{15}N, 13.35 MeV)	14	ε = 35 %	$> 3\cdot10^6$	$> 6\cdot10^9$
NRA (^{19}F, 6.418 MeV)	7	ε = 35 %	$> 1\cdot10^8$	$> 2\cdot10^{11}$
NRA (^{19}F, 16.44 MeV)	17	ε = 35 %	$> 1\cdot10^7$	$> 2\cdot10^{10}$
NRA (^{7}Li, 3.07 MeV)	4	ε = 35 %	$> 2\cdot10^8$	$> 3\cdot10^{11}$

Note that the detection cross section is much smaller than both the ionisation and the displacement cross sections. This illustrates that low sensitivity is not achievable if all hydrogen atoms are dislocated or freed before they are detected in the experiment. The damage number for p-p scattering is low in comparison with other ion beam techniques (as seen in table 3.3), which makes sensitive hydrogen microscopy possible.

There are two reasons for this:
1. The transmission geometry allows a large solid angle behind the sample.
2. The elastic scattering cross section is, for the useful angles, almost two orders of magnitude higher than the cross section of pure Coulomb scattering.

3.2.3 Depth profiling

Surface contaminations are frequently present at higher concentrations than the hydrogen to be analysed, for example in minerals or metal foils, as is also reported by others [25,37]. Reiche et al. report on observations of surface peaks in ERDA, which are suspected to be not due to hydrogen adsorbed on the specimen, but rather to residual hydrogen in the chamber atmosphere in the form of water. According to them, the presence of surface peaks can be linked to the quality of the polishing of the minerals [39]. Another source of contamination could be hydrocarbons from the vacuum pumps. No contamination build-up over time has been observed during experiments, but this process may be fast in comparison to the time the sample spends in the chamber before the start of the analysis. Because of this contamination problem, the total hydrogen content averaged over the whole sample thickness is not representative of the bulk content. Concentration profiling with micrometre depth resolution is essential to selectively analyse the hydrogen concentration in the bulk of a specimen, without the influence of hydrogen adsorbed on the surface. The need for depth profiling capabilities is evident in the case of studies of diffusion profiles, if the sample cannot be cut along the diffusion direction.

3.2.4 Conclusions for the choice of ion beam analytical technique for hydrogen analysis

ERDA is especially advantageous for the detection of light elements in a heavy matrix. The cross sections are enhanced for light projectiles (e.g. ^{4}He), but limited by the standard use of detectors with small solid angle (a few msr). This has a negative effect on the beam damage number. The analytical depth is limited to a few μm, but offers a depth resolution better that 1 nm in the surface. However, in glancing angle geometry the probing depth is less than 1 μm and due to the shallow angle the beam spot is unnecessarily enlarged. [40]

NRA generally has a relatively small cross section, with the exception of resonances, and thus large damage numbers (table 3.1 and 3.3). Sharp resonances, e.g. (^{15}N,αγ) are suitable for depth profiling. However, the depth resolution deteriorates quickly due to the stopping of the incident particle, and thus only a thickness of a few micrometres is realistic. Furthermore, this approach is relatively slow and neither ^{15}N nor energies higher than 3 MeV are available at the Lund Nuclear Microprobe.

Elastic p-p scattering offers the highest cross section and the lowest damage number compared to the other ion beam techniques discussed. The transmission geometry puts a limit on the sample thickness and the depth resolution is not as good as for ERDA and NRA, but is sufficient to distinguish bulk hydrogen from surface contaminations. Thus, elastic p-p scattering can be considered to be the most advantageous technique for hydrogen analysis in order to fulfil the requirements listed above.

3.3 Experimental method for hydrogen analysis at the Lund NMP

3.3.1 Sample preparation technique for minerals and bentonite
The transmission geometry and the limited range of the protons, restrict the analysis to thin, self-supporting samples. The maximum analytical depth decreases with the thickness of the sample, but analysis is possible as long as the sample is thin enough to allow transmission.

For the analysis of minerals, the mineral grains are embedded in plastic and polished until the sample thickness is 10-15 μm. The remaining plastic is dissolved in acetone and the crystal is transferred and attached to an aperture, as shown in figure 3.6. There is a risk that the preparation method may either hydrate the fresh surface or induce microscopic imperfections, which could retain H_2O or hydrous products. Analyses indicate that preparation-induced hydration is normally not a problem below 1000 Å depth [41].

Figure 3.6. *Mineral sample mounted on aperture*

Hydrous and nominally anhydrous natural minerals as well as a synthesized sample with zonations were included in the investigation. The production process of the synthesized sample is described in paper II.

The sample preparation process for bentonite clay is described in detail in paper IV and briefly in chapter 4.4.1. The bentonite samples are analysed also with both the STIM and the PIXE technique, but the hydrogen analysis sets the strictest conditions on the maximum sample thickness. The bentonite cannot be sectioned or polished in the same way as minerals, since the clay is porous and consists of a mixture of the mineral montmorillonite and accessory minerals. Since investigation of this porosity is the aim of the analysis, the structure of the constituents must be maintained in the sample preparation process. Therefore the bentonite is dispersed in water, and then distributed in a mould, where it is dried into a film of clay of suitable thickness.

Mylar foils, $C_{10}H_8O_4$, of different thicknesses (single or multiple layers) were used as standard samples. Mylar exists in many different thicknesses and the hydrogen is homogeneously distributed in depth, but like other polymers, it is known

to be sensitive to ion beam damage, which can lead to considerable elemental losses.
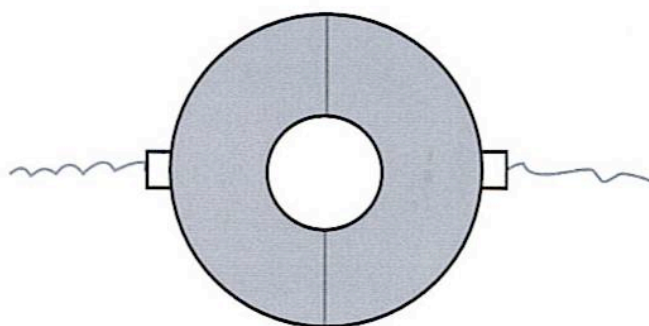
Also samples of the sheet silicate muscovite, were cleaved into standard samples of appropriate thickness. Muscovite was considered to be a better standard, since it is a geological material just like the minerals being analysed, and hence has better matrix similarities than the Mylar foils. Differences in the degree of multiple scattering can affect the coincidence yield, and thus the use of a mineral as standard is preferable. The lower hydrogen content (0.46 wt%) however, made it more time-consuming to routinely use them as standards.

3.3.2 Experimental setup

To take advantage of the full interference-free angle interval and maximise the solid angle, a specially dedicated annular silicon surface barrier detector is used for the hydrogen analysis. The detector is divided into two halves, which are read out simultaneously. It covers a solid angle of 1.5 sr in ideal position, covers angles from 35° to 55° on both sides of the beam direction and has an α-resolution of 25 keV. The count rate was kept lower than 20 kHz in each half of the detector to prevent pile-up effects and an excessive rate of accidental coincidences.

Figure 3.7. *Hydrogen detector manufactured by Ortec. 12 mm hole diameter, 450 mm² sensitive area.*

From the hydrogen measurement, the sample thickness, if unknown, can be determined from the energy sum spectrum. Another way is to perform simultaneous off-axis STIM analysis, where the spectral information can also be used to examine sample homogeneity and normalise the charge. A far better charge normalisation is obtained by directly measuring the charge in a Faraday cup. The charge measurement system at the sub-micron beamline has already been described in chapter 2.4.3. This system, where the beam is deflected into a pre-sample Faraday cup, is far more reliable than the conventional procedure of measuring the charge of the transmitted particles and/or charge from the sample. For geological samples, charge measurement from the sample stage is not applicable because of the poor conductivity of most such samples. Also the secondary electron emission induced by the ion beam complicates the measurements, and the benefit of a method to measure the charge, independent of the sample is obvious.

An example of a typical electronic setup is shown in figure 3.8. The energy signal from each half of the detector is amplified and the elastic scattering events are identified and picked out with a SCA (*single channel analyser*). Both branches are then tested for coincidence within a 200 ns time window. The relative detection time is measured by using the coincidence output as start signal to a TPHC (*time to pulse-height converter*) and the delayed signal from one of the halves as stop signal. Time and energy spectra are acquired with peak-sensitive ADC's (*analog to digital converters*) and recorded in list mode. Data analysis can be performed on- or

off-line with the Kmax software package [42] with a special 8-parameter system (12-parameters when another 4-channel ADC was recently installed), which determines the energy sum and energy difference of coincident detector signals.
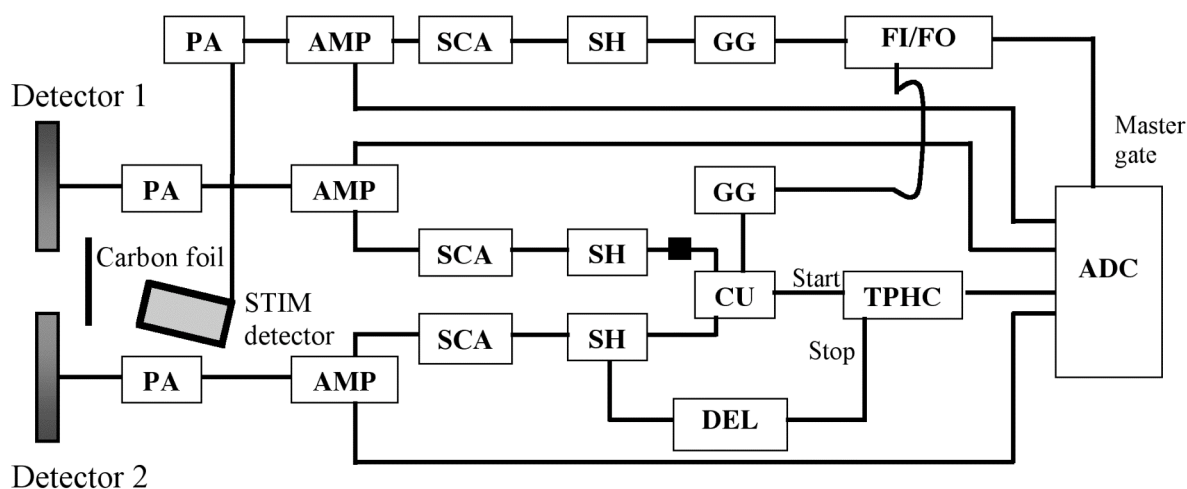
Figure 3.8. *Electronic setup for hydrogen and STIM analysis.*

PA= pre-amplifier   SCA=single channel analyser (zero crossing trigger)
AMP=amplifier   SH=shaper (leading edge discriminator)
DEL=delay   TPHC=time to pulse-height converter
CU=coincidence unit   FI/FO=fan in /fan out
GG=gate generator   ADC=analog to digital converter
■ = small delay

3.3.3 Data evaluation

Coincidence and energy analysis
All events, recorded in list mode, can be sorted with successive time and energy filters. The time information is a tool to distinguish true proton-proton scattering from elastic or inelastic scattering against matrix atoms, or other reactions, which accidentally reach both detectors within the 200 ns time window. This background is directly proportional to the total count rate and is the main contribution limiting the sensitivity. Most of the false coincidences appear in the upper right quadrant in figure 3.9 (b-c), which is a correlation plot between the energy spectra from the two detector halves. Cohen et al. recommend choosing as small a time acceptance window as possible, reducing the beam current and making an energy selection more carefully to reduce the random coincidence rate [28].
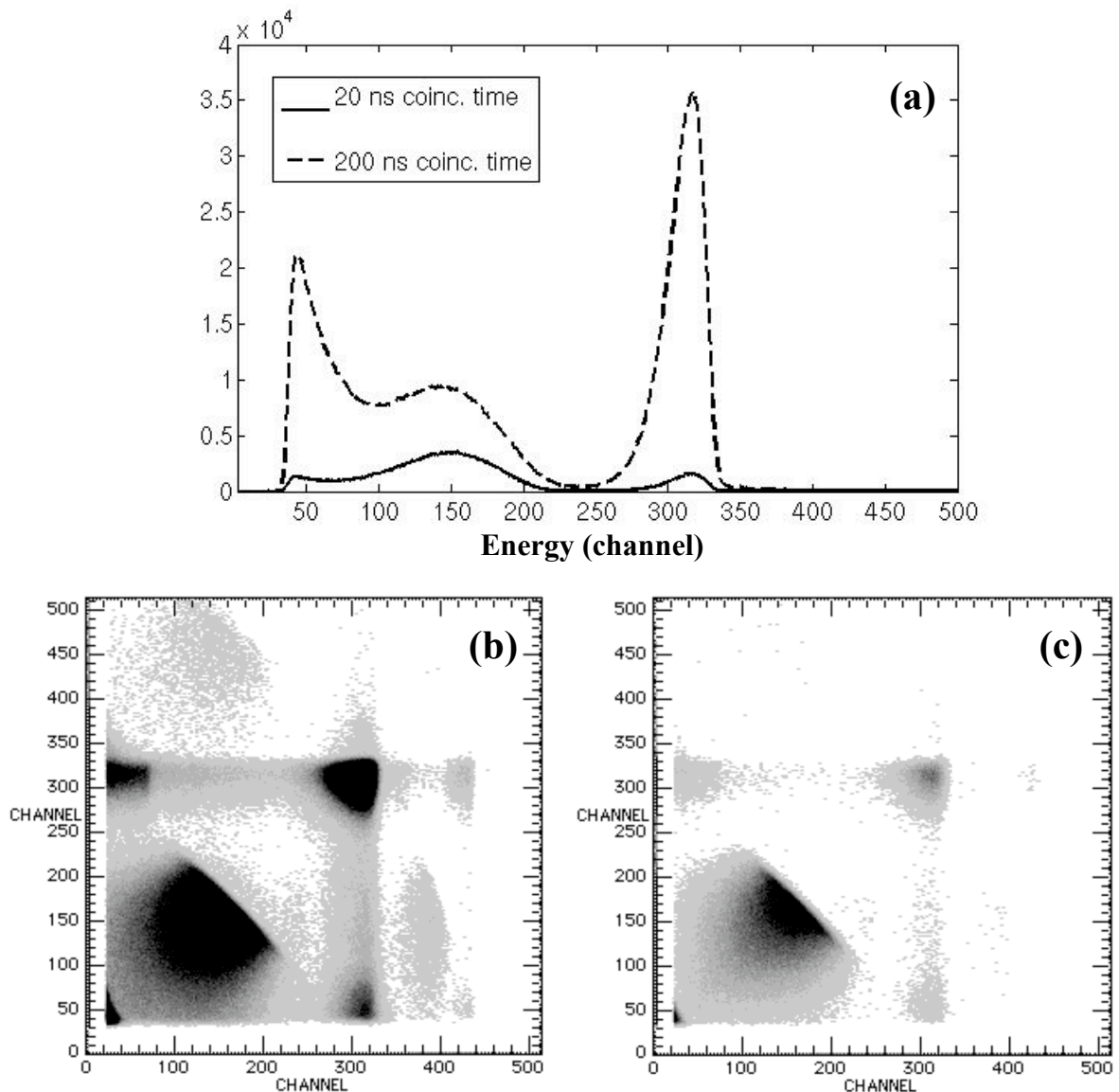
Figure 3.9. *(a) Energy spectrum for detector half "1", with a 200 ns or a 20 ns coincidence window. (b-c) 2D energy spectra of coincident events (energy in detector half "1" against the energy in detector half "2") obtained for a muscovite sample (b) with a 200 ns coincidence window, (c) with a 20 ns coincidence window.*

Figure 3.10 shows a typical time spectrum, with a clear hydrogen peak standing on a continuous background. The background is estimated to 1-2 wt.ppm from a part of the time spectrum which is identified as "not hydrogen". Both positive and negative time difference between a hit in detector half "1" and half "2" can be illustrated because of an applied delay in the electronic circuit scheme in figure 3.8. The coincidence peak is supposed to be much narrower (a FWHM of the order of a few ns) [32], but the poor time resolution is blamed on noise levels that disturb the pulse shape and induce walk-effects.

The acceptable time window is decreased to distinguish true p-p scattering events, which should be detected within a very short time difference. Figure 3.11 shows the "cleaning" effect of decreasing the time window to 20 ns in a plot of energy sum versus energy difference for a Mylar foil between two copper foils. Events in the copper regions are caused by accidental coincidences, but possibly also by true hydrogen contamination. The background is decreased by a factor 4-5 in the copper region when the time window

Figure 3.10 *Time difference spectrum for Mylar.*

is decreased from 200 ns to 20 ns. Also events at unrealistic energies, i.e. outside the sample boundaries in figure 3.11, are considerably reduced.
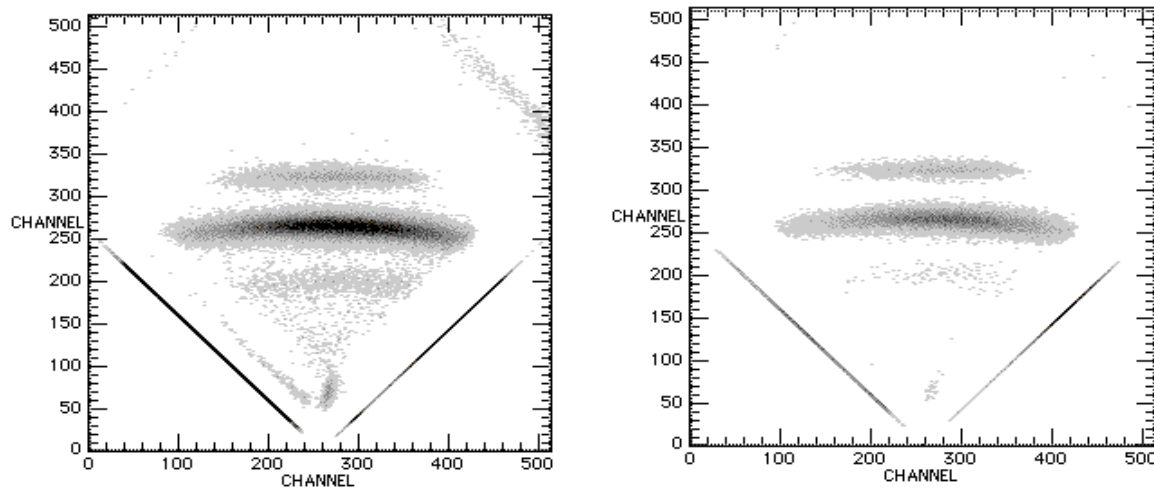
Figure 3.11. *Energy sum against energy difference for 0.9 μm Mylar between 1.7 μm copper foils, with time windows of (a) 200 ns, and (b) 20 ns. Hydrogen contaminations are clearly visible on the copper surfaces as two bands. An offset of 256 channels is applied to the x-axis to allow both a positive and a negative energy difference.*

An even more strict distinction of hydrogen events can be made by putting constraints on the scattering angles. The detector provides no angle information, but simple kinematics say that p-p scattering in 45° results in an energy difference between recoiled and scattered protons equal (or close) to zero.

Summary of filtering conditions:
  1. A hit in both detector halves within user-defined coincidence time (e.g. 200 ns)
  2. An energy sum less than the incident energy ($E_R+E_L <E_{incident}$)
  3. Narrow the time difference interval (e.g. to ±10 ns)

4. (a) Energy difference close to zero → scattering angle = 45°
    or, alternatively
    (b) allow the whole angle interval covered by the detector and determine the
    separate scattering angles

3.3.4 Standards

Determination of the relative atomic hydrogen concentration, ρ_H/ρ_{matrix} requires knowledge of the stoichiometry of the sample as well as the differential cross section at all relevant angles. In this work, the concentrations are instead determined relative to a standard material (Mylar, 4.17 wt.% H or muscovite, 0.46 wt.% H) of corresponding thickness, and are according to standard conventions in geology expressed in wt.ppm hydrogen. Then there is no need for cross sections or knowledge of the sample matrix. Also the positioning of the detector is not crucial, as long as the same settings are used for standards and samples.

Mylar shows no sign of hydrogen loss during irradiation in scanning mode with the micro beam, and is hence approved as standard material. In the case of a 45° scattering angle, a second degree polynomial is fitted to the energy sum spectrum for every standard foil after charge normalisation, see figure 3.12. This polynomial corresponds to the homogeneous hydrogen concentration in the standard sample, and is used as reference for the mineral samples. The charge-normalised energy spectra for sample and standard are then directly compared for relative quantification.
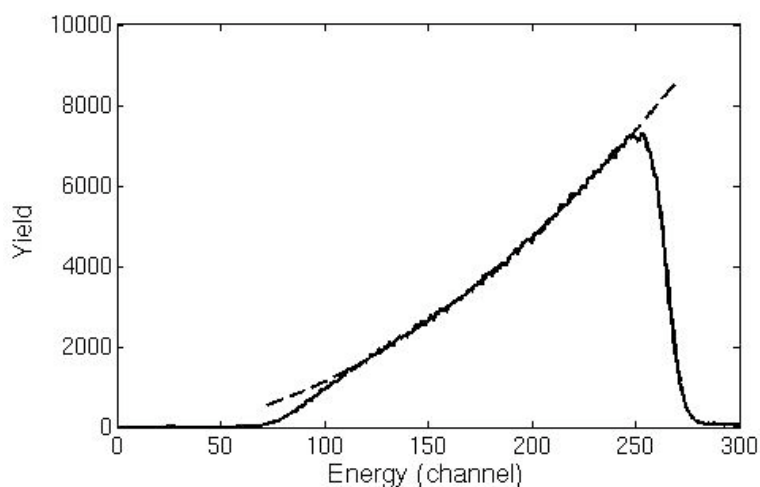
Figure 3.12. *Total energy spectrum (E_R+E_L) for a homogeneous Mylar foil with a fitted 2nd degree polynomial (dashed line).*

In reference [31] the possibility to prepare standard samples by hydrogen ion implantation into various mineral samples is proposed. This could be a useful alternative in situations where it is an advantage to have a strong similarity between standard and sample, both in matrix composition and hydrogen concentration.

3.3.5 Depth profiling

Concentration profiles can be produced with a knowledge of the energy loss experienced by the protons and the scattering angle. This is easy if the analysis is restricted to scattering angles of 45°, where the energy of the incoming proton is equally divided between recoil and scattering product. The energy sum of the right and left detector halves can in the case of scattering through 45° be written as

$$E_R + E_L \approx E_{incident} - \int_0^x \left(\frac{dE}{dx}\right)_0 dx - 2 \int_0^{\sqrt{2}(d-x)} \left(\frac{dE}{dx}\right)_1 dx \qquad (3.8)$$

for scattering at the depth x in a sample of thickness d. The 45° requirement was used in the introductory experiments described in paper I, and simplifies the depth profiling. The recoiled and the scattered protons travel the same distance through the sample, with the result that the relative difference in energy is zero, and thus such events can be selected for further analysis. The x-axis (channel) in the energy sum spectrum is converted to energy and the corresponding depth is calculated with a knowledge of the stopping power in Mylar [43] and consideration is taken to the energy loss before the scattering event (denoted with "0" in eq. 3.8) together with the energy loss of the reaction particles after scattering (denoted "1"). The energy stopping before scattering is much less than after the scattering event.
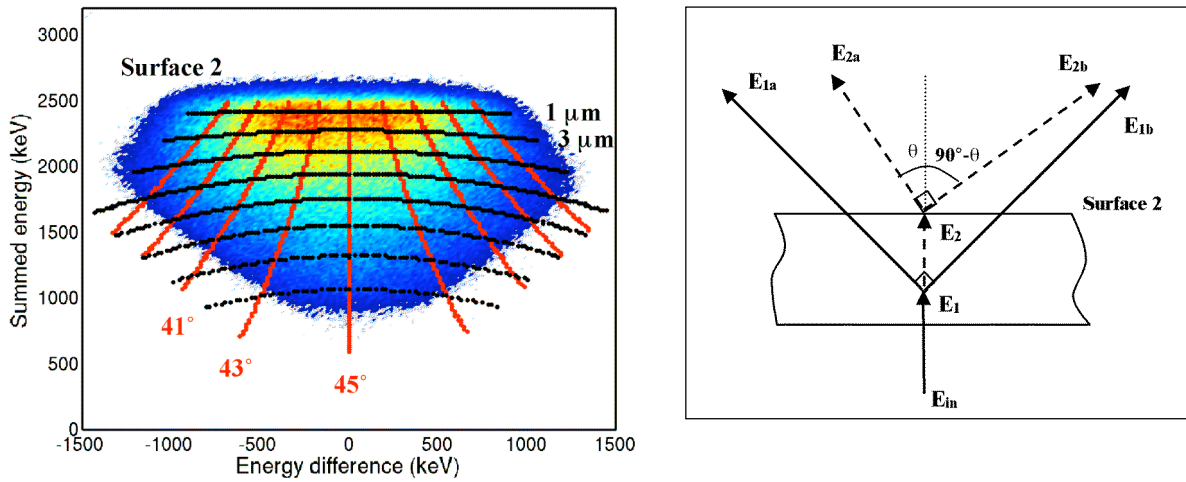
Figure 3.13. *(a) Energy sum (E_R+E_L) against energy difference (E_R-E_L) in Mylar, with superimposed lines corresponding to different depths and scattering angles in steps of 2 μm and 2° respectively. The colour scale in the plot is proportional to the number of detected events, ranging from blue via green and yellow to a maximum in red. Isodepths are represented in black and equal angles in red. Figure (b) is intended to explain (a) and illustrate the origin of events.*

Limiting the analysis to 45° only, reduces the available statistics significantly. All angles covered by the detector (35°-55°) can be used, but since the detector provides no angular information, it is then necessary to determine the scattering angle by an indirect approach by using the energy information (paper II). According to the literature, such indirect angle determination is by far more accurate than using a

position-sensitive detector [38] and a total relative depth resolution of less than 10% can be achieved. Therefore this is not a disadvantage. Figure 3.13 illustrates how the scattering angle or depth can be determined from a plot of the energy sum versus the energy difference. The top surface has a constant summed energy, which arises from scattering in the surface facing the detector (E_R+E_L nearly constant). The bottom surface is curved because of the larger energy loss and energy difference at larger scattering angles, due to the angle-dependent path length and division of energy.

Hydrogen analysis is restricted to thin samples, due to the limited range of 2.5-2.8 MeV protons. Concentration profiling is only possible down to depths at which both the recoiled and the scattered protons have energy enough to reach the detector. The maximum analytical depth depends on sample thickness and scattering angle, as different scattering angles have different path lengths through the sample, and is illustrated in figure 3.14. Maximum profiling depth is reached with a scattering angle of 45°, since this induces the smallest energy loss.

The depth resolution is affected by extrinsic effects (energy and angular spread of the beam and detector resolution) and intrinsic effects (energy straggling and multiple scattering) [37,40]. As mentioned above, a relative depth resolution of less than 10% can be expected. This is illustrated in figure 3.15 (a), where the surface contamination on a 0.8 μm thick aluminium foil is separated, and in (b) with 0.9 μm Mylar between 1.7 μm copper foils (also with surface contaminations) is also well resolved. The left-hand peak (at lower energy) is broader than the right-hand one, and is a result of energy straggling and multiple scattering in the sample. Multiple scattering induces energy and lateral beam spread. This is not a problem for the incident ions, since the angle between the recoiled and the scattered particle is still 90 degrees. Multiple scattering of either the scattered or recoiled particle however, leads to a deviation from the 90° condition, so that one of the particles has a chance of missing the detector, thus reducing the coincidence yield. This effect is, however, reduced if a large solid angle detector is used.
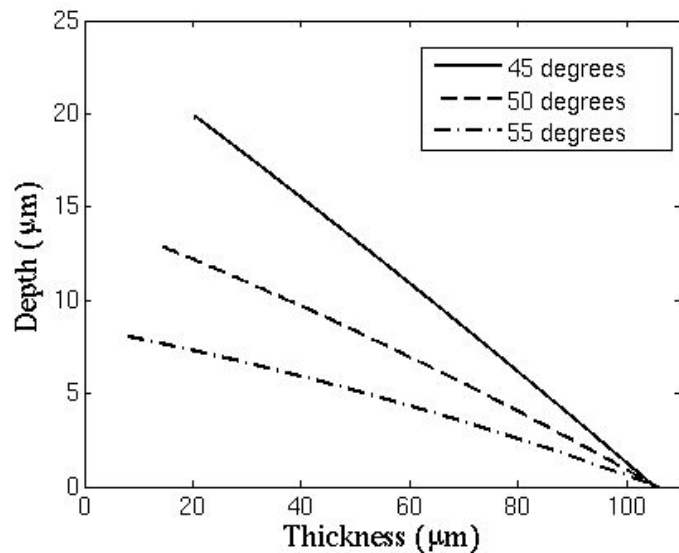
Figure 3.14. *Maximum analytical depth for varying sample thickness (Mylar) at 45°, 50° and 55° scattering angle, with an incident proton energy of 2.8 MeV.*
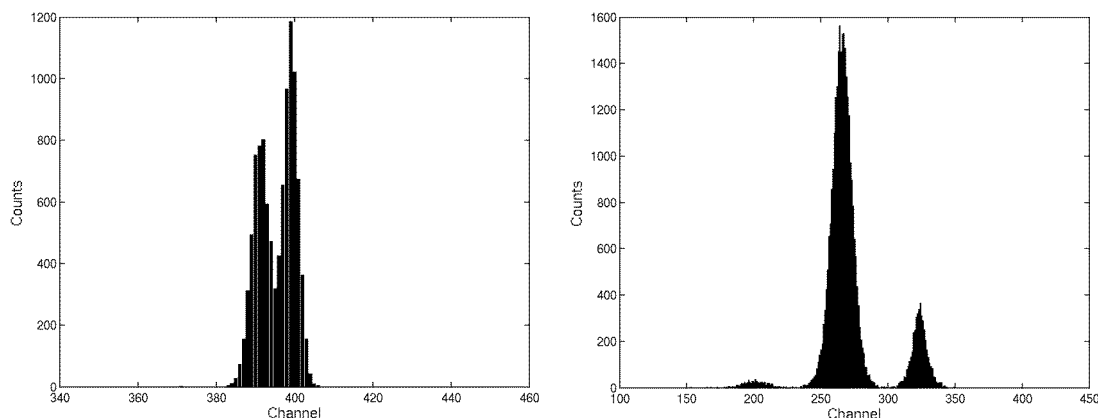
Figure 3.15. *(a) Surface contamination on a 0.8 µm thick aluminium foil (FWHM=0.4 and 0.5 µm resp.) (b) 0.9 µm Mylar between 1.7 µm copper foils. The left-hand and right-hand peaks correspond to surface adsorbed hydrogen (FWHM=1.4 and 2.4 µm).*

3.4 Application areas of hydrogen analysis

Hydrogen is an important element, which is present everywhere as a component of, for instance, water and hydrocarbons. It is often found as a surface contaminant on metals. What makes hydrogen so interesting is that even at low concentrations, it can affect the properties of a material to a high degree. Especially in semiconductor physics etc, hydrogen plays a big role as charge carrier.

It is very common to measure the diffusion of hydrogen into semiconductor materials by ERDA [44], but naturally the analysis is then concentrated to the surface region. For bulk analysis, e.g. in polycrystalline, CVD-grown diamond, the p-p scattering technique has recently been used to quantify the enhancement of hydrogen at grain boundaries. Proton-proton scattering is the only method that is capable of measuring these low concentrations reaching down to a detection limit of 0.08 at.ppm [24,27]. Another application area is found in environmental science, where hydrogen analysis is often performed in macro mode. Hydrogen depth profiling, in combination with other ion beam techniques, has been performed on quartz air filters in order to determine the total amount of particulate organic matter in aerosols [45].

In geology, hydrogen analysis plays an important role to gain knowledge of how minerals evolve, of how exchange reactions are driven, and about the water budget in the interior of the Earth as well as the fluence of water. Other examples in geology are hydrogen analysis of melt inclusions to understand the dynamic mechanism of magmatic activities [31]. Since the main application area for the hydrogen analysis presented in this thesis was within geology, I will give a brief geological background, a framing of the question and aim of the analysis in the following paragraph. As described in paper IV, hydrogen analysis was also performed on bentonite clay samples, in order to evaluate this as a suitable method to measure the degree of water saturation in the clay. A motivation and description of the questions at issue concerning bentonite are addressed in chapter 4.4.1.

3.4.1 Geological background and motivation

For geologists, the presence of hydrogen in minerals in the crust of the Earth is of importance due to its dramatic influence on the physical properties of the mantle; for example on the melting point, viscosity and elastic properties such as the seismic velocity. Plate tectonics is only possible if the water content of the mantel is above a threshold value, and the difference in tectonic style observed on Mars and Venus may therefore be directly related to differences in mantle water content [46]. There is at least as much water in the interior of Earth as in all its oceans together, mostly in the form of OH-molecules in the mantle minerals. This water was captured from water vapour in the gas cloud that Earth was born from, and has been stored since then. Signs of this hidden water can be found in meteorites or material that has been transported to the Earth's surface by volcano eruptions or through erosion.

During recent years, it has become evident that several of the *nominally anhydrous minerals (NAM)* in the Earth's mantle contain low but significant hydrogen concentrations. The nominally anhydrous minerals do not contain hydrogen in their structural formula, but hydrogen is present as point defects in the crystal structure in the form of OH^- ions or less commonly as H_2O [47]. The concentrations range from a few to thousands of wt.ppm H_2O in natural minerals (mantle minerals like olivine, pyroxene, garnet etc.) [23,48]. 95% of the upper mantle minerals are NAM and, due to the large dimension of the mantle, these phases work as an enormous water reservoir. The amount of hydrogen that is incorporated in these phases is quite sensitive to pressure and generally increases with pressure and sometimes with temperature [46].

The diffusive nature of hydrogen, combined with its ability to take part in exchange reactions with other elements [49] creates an internal water cycle in the Earth. As an example, nominally anhydrous phases can carry as much as $1.1 \cdot 10^{11}$ - $7.8 \cdot 10^{11}$ kg H_2O per year into the deep mantle through subduction zones [23]. Within the subduction slab, pressure and temperature increase as the slab subducts. This causes the dehydration of aqueous minerals and results in the generation of aqueous fluid. The aqueous fluid is thought to ascend, due to buoyancy, along solid grain boundaries or through cracks. The understanding of this system is still limited, since most studies have been performed in the past ten years. Quantification of hydrogen concentrations in mantle minerals, combined with studies on dynamic processes in the mantle (e.g. diffusion, hydrogen exchange reactions and solubility) is a step towards a more detailed understanding of this complex system.

The main analytical method for studies of hydrogen in nominally anhydrous minerals has been *Fourier transform infrared spectroscopy (FTIR)* [47,48]. The method is based on the characteristic absorption of frequencies in the IR regime, due to vibration resonances in hydrogen bonds. This method has high sensitivity (a few wt.ppm H_2O) and the characteristic absorption bands yield information about the kind of hydrogen bond, the chemical environment and whether it is atomic or molecular hydrogen, and can thereby distinguish between structurally incorporated hydrogen and adsorbed water, fluid inclusions etc. The intensity of the absorption peak is a measure of the hydrogen concentration. However, for quantitative hydrogen analysis the absorption cross section for IR radiation must be known, as well as the extinction coefficient, which is not the case for all materials. FTIR can distinguish bonding types and different molecular groups, but cannot give information on the

unbound hydrogen. For these reasons, calibration against an independent, complementary technique is required [41].

There are several other techniques for hydrogen analysis at low concentrations, e.g. secondary ion mass spectrometry (SIMS), the bulk techniques H MAS (magic-angle-spinning) NMR spectroscopy and gas-extraction methods. However, these methods involve other problems, such as strong matrix effects, difficulties to avoid surface water and inadequate detection limits. NMR could be a useful complement to FTIR, since it can detect also unbound hydrogen species in a sample. However, the limited sensitivity together with the requirement of complicated instrumentation and that the samples must be free of paramagnetic ions, such as Fe^{2+}, has had the result that NMR is not commonly used for hydrogen analysis in minerals.

Minerals often have an inhomogeneous structure with fluid or gaseous inclusions, which makes measurements with micrometer resolution necessary. Another major question is whether the hydrogen concentrations observed in mantle-derived samples represent the original concentrations, or if hydrogen may have been lost during the ascent process. The diffusion coefficients can vary by orders of magnitude between minerals, and therefore some minerals may have lost most of their water during ascent while other minerals may have preserved their original water content [46]. Therefore it would be highly desirable to directly deduce the water content in the mantle from geophysical data, for example, by remote sensing using electric conductivity data, instead of relying on samples of ascended mantle mineral.

If significant changes in the hydrogen concentration have occurred during the ascent process, this could possibly be observed as diffusion profiles by techniques offering spatial resolution in the micrometre-range. Here ion beam analytical methods, especially with the use of micro or nano beams, provide a valuable alternative. Elastic proton-proton scattering is considered to be the most suitable method to fulfil the requirements of high sensitivity measurements suitable for analysis of nominally anhydrous minerals, as well as depth profiling, to be able to distinguish bulk hydrogen from surface absorbed contaminations, as discussed in previous paragraphs. Figure 3.16 shows examples of hydrogen depth profiles in minerals; (a) amphibole and (b) orthopyroxene with a distinct surface contamination peak.
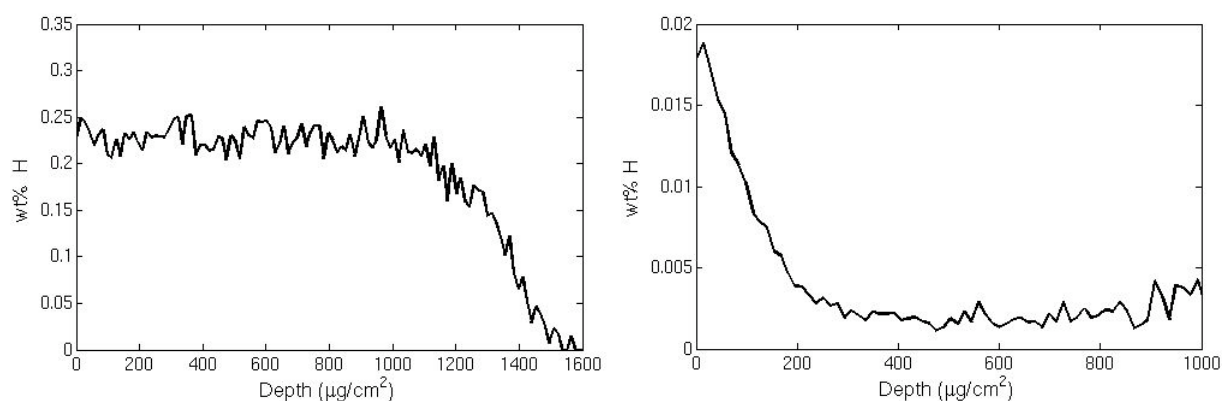
Figure 3.16. *Hydrogen profiles of (a) amphibole and (b) orthopyroxene with a distinct surface contamination peak.*

Some mineral samples that have been analysed are listed in table 3.4 together with approximate hydrogen concentrations and a classification.

Table 3.4. *Sample selection with approximate hydrogen concentrations.*
NAM – nominally anhydrous mineral.

Mineral sample	Hydrogen content (wt.ppm)	Classification
Muscovite	4600	Hydrated (standard)
Tourmaline	2800	Hydrated (standard)
Amphibole	2000	Hydrated (standard)
Garnet	100, 340	NAM
Orthopyroxene	21	NAM
Diopside	20, 10	NAM
Synthetic orthopyroxene	40	Synthetic NAM

3.5 Future development

3.5.1 The charge normalisation problem

A problem frequently encountered in hydrogen analysis has been the uncertainty in the charge normalisation. Different methods for charge normalisation have been tried, among them, charge collection in the post-target Faraday cup, the Faraday cup in combination with the sample wheel, the STIM technique and lately in a pre-target Faraday cup. The post-target Faraday cup measurements turned out to give highly irregular results for series of standard samples with increasing thickness even at short irradiation times, where beam damage effects or the addition of hydrogen is not expected. STIM measurements turned out to be more trustworthy, but still not perfect. After the installation of the pre-target Faraday cup, the charge normalisation is now totally independent of sample composition and thickness. Also potential scattering and electron escape from the sample cannot affect the charge measurement, and it is considered to be much more reliable. However, anomalies are occasionally observed in the series of standard samples. Investigations on the possibility of count rate induced problems and insufficient dead time corrections have still not answered all the questions. This problem must be solved before reliable hydrogen quantification can be performed. There is so far no explanation for this behaviour

3.5.2 3D-profiling

The possibility of three-dimensional concentration profiling is briefly investigated in paper II, in the analysis of a diffusion profile in a synthetic sample. Since each point of interest must contain sufficient statistics for a depth profile, the analysis becomes extremely time-consuming if the hydrogen concentrations are low. It is concluded that it is possible, but a balance between reasonable beam time, beam damage effects, spatial resolution and detection limits must be found. Data evaluation also becomes time-consuming and requires optimisation of the depth profiling procedure. Analysis of samples with inhomogeneous hydrogen content would indeed be interesting, but

3D-profiling within a reasonable beam time is not possible for concentrations on the ppm-level, and therefore it is not a practical choice for nominally anhydrous minerals.

3.5.3 Position-sensitive detector

The experiment could gain from the use of a detector with a larger area. The solid angle could be made even larger and reduce the irradiation time, or the sample-detector distance could be increased with maintained solid angle to relieve the tight positioning conditions inherited with the standard detector.

Trials with a new position-sensitive semi-conductor detector are planned in the next experiments. This detector is divided into 32 concentric rings on the front side and 64 sectors on the back, and would provide interesting information on the position of every particle that is detected. It has already been concluded that this kind of information does not provide better depth location information than what can be determined with energy loss calculations with the old detector setup, but it would be more sophisticated and the old detector needs to be replaced due to irradiation damage and aging.

Ion beam microtomography

The concept of non-invasive examination of the inside of an object was born with the discovery of X-rays by Wilhelm Conrad Röntgen in 1895. In his famous radiograph of his wife's hand, the contrast reveals bone, soft tissue and her ring, as a consequence of material-dependent X-ray absorption due to different electron densities. The image is a projection, and illustrates the complex superposition of the attenuation through the object. As a consequence of the superposition of tissues above and below an area of interest, the depth information is lost and it requires a trained eye to distinguish structures with small differences in attenuation coefficient for accurate medical diagnostics.

In 1972, with the realisation of the first CT-scanner by Godfrey N. Hounsfield at EMI, it became possible to create cross sections of an object, and study the internal variations in attenuation coefficient without the loss of depth information. Hounsfield was awarded the Nobel Prize in Physiology or Medicine in 1979 together with Allan Cormack, who, in the early 1960's, presented CT (computerised tomography) as a new approach for imaging. The mathematical theory behind this technique however, had been developed already in 1917 by the Austrian mathematician Johan Radon.

Today, tomography is used in many diverse research areas and in industry to perform non-destructive examinations and gain cross sectional or true three-dimensional information on test objects. Not only X-rays are used for the imaging, but also other kinds of electromagnetic waves or particle radiation. The impressive range in object size stretches from proteins imaged by NMR/MRI to investigations of the interior of the Earth by seismic tomography.

The traditional, two-dimensional mapping with ion microprobes, was extended to tomographical investigations in the mid 1980's, independently by several research groups [50,51]. By exploiting the full three-dimensional information, small structures inside samples can be imaged, e.g. cellular structures or porosity, without the problematic superposition of information found in two-dimensional "flat" imaging. Tomographic investigations are time-consuming and require very small sample dimensions, and have therefore not replaced standard, two-dimensional mapping, which delivers sufficient information in most applications. For specific questions at issue however, tomography can be a source of valuable information, which simplifies the interpretation of data and makes features visible, which cannot be distinguished in only two dimensions.

In the first part of this chapter, the basics of tomography are explained, together with a description of different algorithms that can be used for image reconstruction from projection data. The diversity of existing tomography methods is illustrated by a number of examples. The second part of the chapter deals with ion beam tomography, describing the setup at the Lund Nuclear Microprobe and the

procedure for the execution of a STIM tomography experiment is described, together with results from real data reconstructions.

4.1 The principle of computed tomography

The word *"tomography"* originates from Greek, with the meaning tomo – slice or cut, and graphy – write. An image of a slice, or a cross section, of the object can be derived mathematically, by illuminating the object from many different angles and measuring how the radiation is affected by passage through the object, either in terms of intensity or energy loss. The data on the transmitted energy or intensity, at each specific angle, is denoted a *projection*, and represents the line integral of the measured parameter through the object. This set of projections, taken around the object at a specific height, is called a *sinogram*. By combining a set of projections, commonly acquired at intervals through 180 or 360 degrees around the object, a *reconstruction* of the object can be produced by applying different mathematical algorithms. By stacking many of these reconstructed cross sections on top of each other, a full three-dimensional image of the object can be produced.

The radiation source can be treated as a parallel or divergent beam – called a fan or cone beam in the latter case, and the source can be placed either inside or outside the object. Also the detector can have different positions*: transmission or reflection geometry*. Examples of these different source-detector configurations are presented in figure 4.1. The variety in source-detector configurations and different sources of irradiation has given rise to a number of famous diagnostic techniques, such as PET, SPECT and MRI. This wide variety of methods, have the basic technique in common, but a number of different parameters are measured and imaged and there are even real-time methods for studies of metabolism and organ functions.
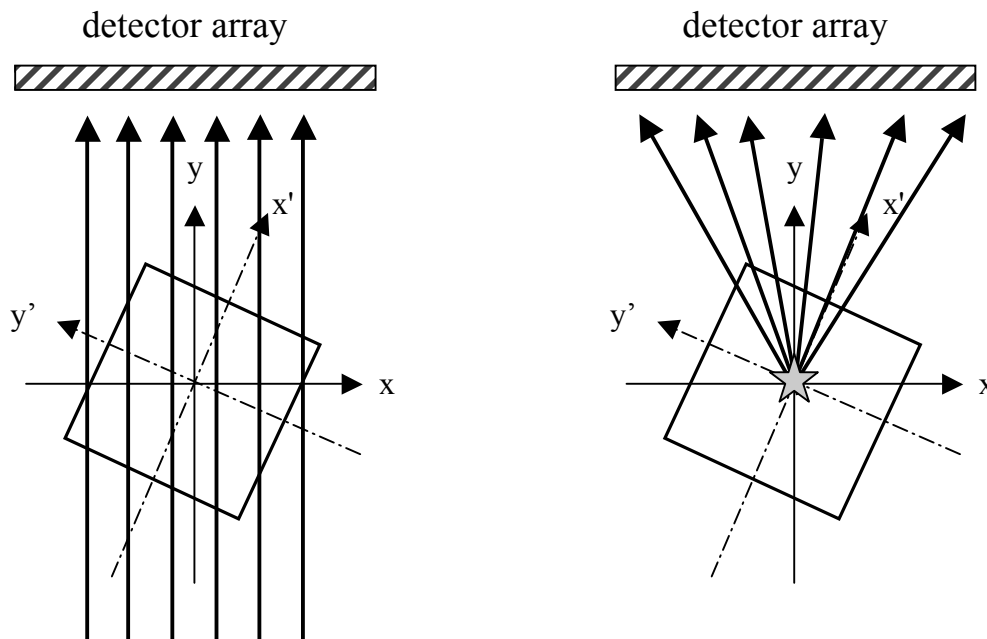
Figure 4.1. *Parallel beam in transmission geometry (left) and fan beam in emission geometry (right).*

4.1.1 Different geometries for tomography

In the first applications of computerised tomography, X-rays were used to form pictures of the X-ray attenuation coefficient. Today it is possible to produce images also with radioisotopes, ultrasound, magnetic resonances etc., with different parameters imaged in each case. With the introduction of the 3rd generation synchrotrons, which are capable of producing a highly coherent radiation, common X-ray tomography has been extended to involve also phase contrast imaging, which makes it possible to resolve structures with low absorption contrast. Other attractive features are short exposure times and micrometre resolution [52,53].

Here a brief summary is given of some popular kinds of tomography, with a basic description of the method together with some useful terms etc. The categorisation can be made with respect to source-detector geometry or the radiation source.

Transmission tomography

The most common example of transmission tomography is X-ray tomography, where the projections represent the line integrals of the attenuation coefficient of the material. The benefit of X-rays in transmission geometry is that they can penetrate large objects, since they do not experience energy loss in their propagation through matter, but are only attenuated in intensity.

For diagnostic imaging in medicine, 20-150 keV X-rays are used as radiation source. In this energy range, X-rays interact with matter via the photoelectric effect or Compton scattering, which cause a decrease in beam intensity. These two processes are energy-dependent and as a result also the attenuation coefficient is energy-dependent. Since X-rays of low energy are more attenuated than those of higher energy, a polychromatic beam becomes enriched in high energy when passing through a sample – a process called *beam hardening*. Therefore, one should use a monochromatic beam or use detectors that measure both energy and intensity. The detector should also be collimated to allow the assumption of parallel beam propagation and to avoid scattering.

There is also a variety of optical methods by which the optical properties are measured. One interesting example is fluorescence mediated tomography [54], in which fluorophores are used as contrast agents inside tissue, and measurements are performed both on transmitted excitation light and fluorescence light.

STIM tomography, which is the type of tomography that has been experimentally executed in this thesis work, exemplifies the use of ions as radiation source. In comparison to X-rays, the penetration of MeV ions is very limited, and thus this technique can be applied only to microscopic samples.

Emisson tomography

The decay of radioactive isotopes can be used to image the distribution of the isotope in real-time by detecting its emitted radiation. In this way the path of the isotope can be traced through different organs, to study metabolism or uptake of a medication. The source is assumed to be an isotropic point source with a suitable decay time, and its radiation is detected in an array or ring of detectors around the object/patient.

Examples of emission methods are PET (*positron emission tomography*), SPECT (*single photon emission CT*) and MRI (*magnetic resonance imaging*), where MRI is more complicated and quite different from the other techniques.

In SPECT imaging, gamma rays from a radiopharmaceutical with a suitable decay time are detected with a gamma camera that is rotated around the patient.

In PET a β^+-decaying isotope is administered, and the two counter-directed gamma rays from the subsequent annihilation are detected. Low positron energy is essential since the annihilation has to occur close to the source. The two gamma rays are detected in coincidence, and the point of emission is localised on a line between the two detectors.

MRI is based on the fact that many atomic nuclei have a magnetic moment, spin, and if the atom is placed in a strong magnetic field, the moment tends to line up with the magnetic field. If a radiofrequency field is applied, some nuclei will flip their orientation and emit a signal when they later return to their equilibrium state. This signal can yield information on both the type and concentration of atoms and the chemical environment. For tomographic investigations, the position of the emitting nucleus must be known. This is achieved by applying variable magnetic field gradients, which change the magnetic field so that all points along a line get their own magnetic field intensity.

Reflection tomography

In cases when the transmitted signal cannot be measured, e.g. in situations with large attenuation losses, the reflected signal can be used instead. A common method, which utilises reflection geometry, is ultrasonic imaging. Common pulse-echo ultrasound is limited by the fact that only tissue interfaces can be distinguished. Scattering from the bulk may reach the detector, but the scattered sound wave is modified every time it passes a tissue surface, and hence the signal is difficult to interpret. Ultrasound tomography is then an interesting strategy for imaging. For straight ray propagation, one can measure phase shift, attenuation or the time of arrival of the received signal (note that the propagation speed is low in comparison to e.g. X-rays) and image the attenuation coefficient or refractive index of the object. The technique is applicable for soft tissues, where the refraction effects are small, and is used for mammograms, imaging of the heart etc.

Other examples of areas of interest for reflection tomography are in environmental and seismological examinations, e.g. for examination of the "inside of the Earth" [55].

4.1.2 Reconstruction techniques

The basic idea of image reconstruction is to convert the projection data, the sinogram, into an image. There is a large variety of reconstruction techniques, which can be categorised into three basic groups: *algebraic, analytical* and *statistical methods*. Also there are iterative versions of these techniques. The choice of reconstruction technique is based on the speed of the algorithm, how artefacts influence the image quality and the possibility to introduce corrections during the reconstruction to take into account different physical phenomena, such as X-ray attenuation in the case of PIXE tomography.

In the next paragraphs, an overview of these main methods is given with a brief description of their principle together with a discussion of their suitability for ion beam tomography.

Analytical reconstruction techniques

The mathematical solution to the reconstruction problem was completed by Radon in 1917. The method of backprojection was used in the first CT-scanner, and was later also commonly used in radioisotope emission methods. Also today, the more advanced version, filtered backprojection, is one of the most commonly used reconstruction techniques, at least in medical tomography. It is known to be fast, maybe the fastest, and accurate.

In the ideal case, projections are a set of measurements of line integrals of a certain parameter through the object. The object is represented by a function *f(x,y)*, illustrating for instance the linear attenuation coefficient in the case of X-ray tomography. Two different coordinate systems are defined, one fixed in the object *(x,y)* and another that rotates with the source-detector system *(t,s)*.
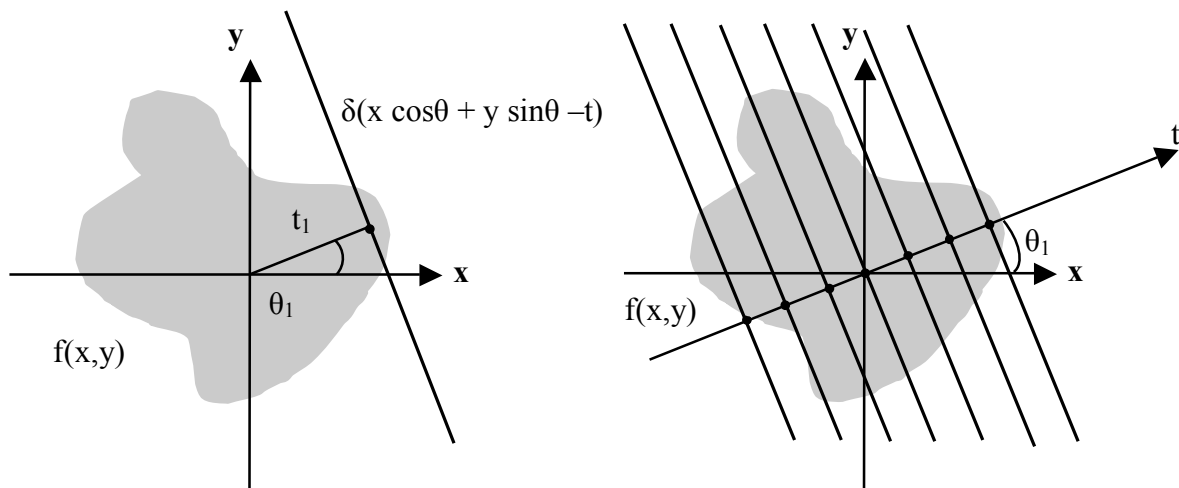
Figure 4.2. *(a) Illustration of a ray that passes through the object and forms a line integral of the object function f(x,y). (b) a set of line integrals for the constant angle θ_1 forms a projection.*

Each line is denoted by the (θ,t) parameters (see figure 4.2), and its equation is described by

$$x\cos\theta + y\sin\theta = t \tag{4.1}$$

The corresponding line integral, $P_\theta(t)$, is described by:

$$P_\theta(t) = \int_{(\theta,t)line} f(x,y)ds \tag{4.2}$$

A projection is formed by combining a set of line integrals, which are obtained by moving the detector-source system along the *t* axis for a constant angle θ (see figure 4.2). In fan beam configurations, the source is fixed and we have a set of detectors along a line or surrounding the object. The mathematical derivation in this chapter

considers only parallel beam geometry and assumptions are made about mono-energetic radiation, a narrow pencil beam and a well collimated detector, which is not hit by scattered radiation.

From the expression of the line integral, the projection of the object at angle θ at distance t is defined by the *Radon transform* of the function $f(x,y)$:

$$P_{\theta}(t) = \int_{-\infty}^{\infty} \int_{-\infty}^{\infty} f(x,y)\delta(x\cos\theta + y\sin\theta - t)dxdy = \Re\left[f(x,y)\right] \qquad (4.3)$$

The Dirac delta function ensures that the integration is carried out only along a line. The projections taken at an angle θ_1 end up along a radial line in the Radon domain, which is illustrated in figure 4.3.
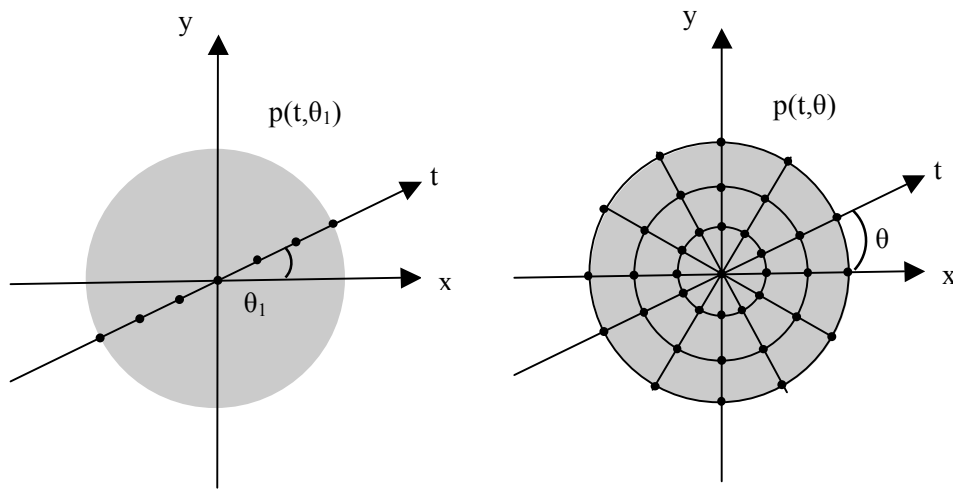
Figure 4.3. *(a) Radon transform for the angle θ_1. (b) Radon transform for many projection angles.*

To calculate the image, i.e. *f(x,y)*, the Radon transform must be inverted using an inverse Radon transform. The Fourier Slice Theorem explains how this can be done, by relating the measured projection data to the two-dimensional Fourier transform of the object cross section [56]. The Fourier Slice Theorem states that the one-dimensional Fourier transform of a parallel projection at a certain angle θ is equal to a radial slice of the two-dimensional Fourier transform *F(u,v)* of the object *f(x,y)*. Hence, the object can be estimated by performing a two-dimensional inverse Fourier transform of the projection data. Support for the following derivation and a motivation can be found in mathematical text books on the subject, such as the book by Kak and Slaney [56].

The 2D Fourier transform of the object is defined as:

$$F(u,v) = \int\limits_{-\infty}^{\infty} \int\limits_{-\infty}^{\infty} f(x,y)e^{(-j2\pi(ux+vy))}dxdy \qquad (4.4)$$

The Fourier transform of a projection at angle θ is defined as:

$$S_{\theta}(w) = \int\limits_{-\infty}^{\infty} P_{\theta}(t)e^{(-j2\pi wt)}dt \qquad (4.5)$$

If the values for $F(u,v)$ are viewed along the line $v=0$ in the frequency domain (equal to the angle $\theta=0$) in combination with equation 4.4 and 4.5, this gives

$$F(u,0) = \int\limits_{-\infty}^{\infty} \int\limits_{-\infty}^{\infty} f(x,y)e^{(-j2\pi ux)}dxdy = \int\limits_{-\infty}^{\infty} \left[\int\limits_{-\infty}^{\infty} f(x,y)dy \right] e^{(-j2\pi ux)}dx = \int\limits_{-\infty}^{\infty} P_{\theta=0}(x)e^{(-j2\pi ux)}dx = S_{\theta=0}(u)$$

$$(4.6)$$

This shows that the values of $F(u,v)$ on the line defined by $v=0$ can be calculated by the Fourier transform of the projection of the object along the y-axis. This result is independent of the orientation of the object and the coordinate system and can be generalised to show that, if $F(w,\theta)$ gives the values for $F(u,v)$ along a line at an angle θ to the u-axis, and if $S_{\theta}(w)$ is the Fourier transform of $P_{\theta}(t)$, then

$$F(w,\theta)= S_{\theta}(w) \qquad (4.7)$$

In other words, the two-dimensional Fourier transform can be determined on radial lines from the one-dimensional Fourier transform of projections at angles $\theta_1, \theta_2, \dots \theta_k$. For an infinite number of projections, $F(u,v)$ will be known at all points in the *uv*-plane and $f(x,y)$ can be determined by inverse Fourier transformation. The Fourier Slice Theorem is illustrated in figure 4.4 together with the procedure for reconstructing $f(x,y)$ from a set of projections.

In practice, only a finite number of projections are known and $F(u,v)$ is known only along a finite number of radial lines. Hence the two-dimensional inverse Fourier transform of $F(u,v)$ cannot be executed in continuous form, but is approximated by its discrete version. The implementation of this discrete approximation is called *backprojection*. Each of the projections is "smeared out", or backprojected, evenly along the projection line and the process is repeated for each angle θ. The contributions from every smeared projection are summed together to produce the final reconstructed image. The principles are shown in figure 4.5. Interpolation must be used to implement the continuous function given discrete data points. The interpolation error becomes larger with a sparser density of radial points, i.e. for high-frequency components, with image degradation as a consequence. It is clear that the number of projections available determines the spatial resolution, and thus the quality of the reconstructed image. Noise and fluctuations in the data set turn up as high-frequency noise after the Fourier transformation, and appear as star-shaped artefacts in the reconstructions. However, these artefacts can be suppressed by

$$f(x,y) = \Im_2^{-1}\Big[\Im_{rad}\big[\Re[f(x,y)]\big]\Big]$$
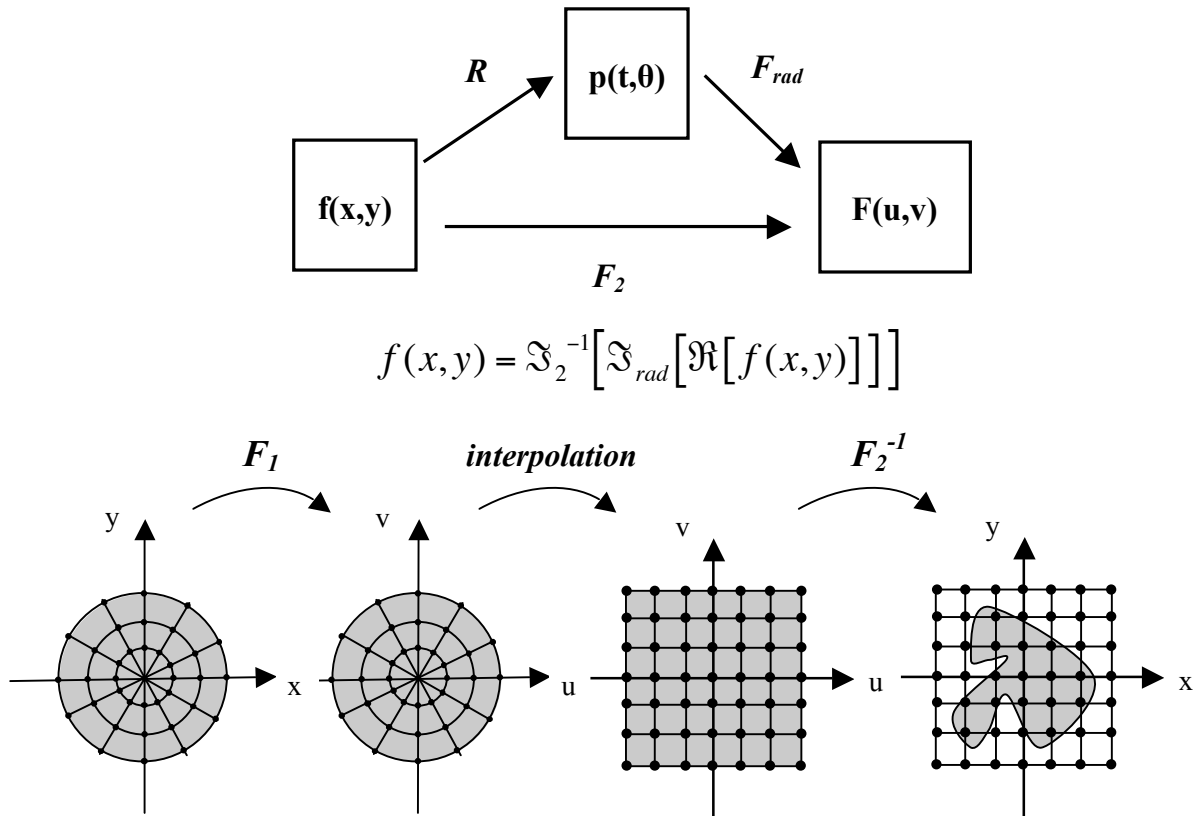
Figure 4.4. *(top) Illustration of the Fourier Slice Theorem. (bottom) Reconstruction procedure, starting with the Radon transform and ending with the reconstructed image f(x,y). Freely from ref [57].*
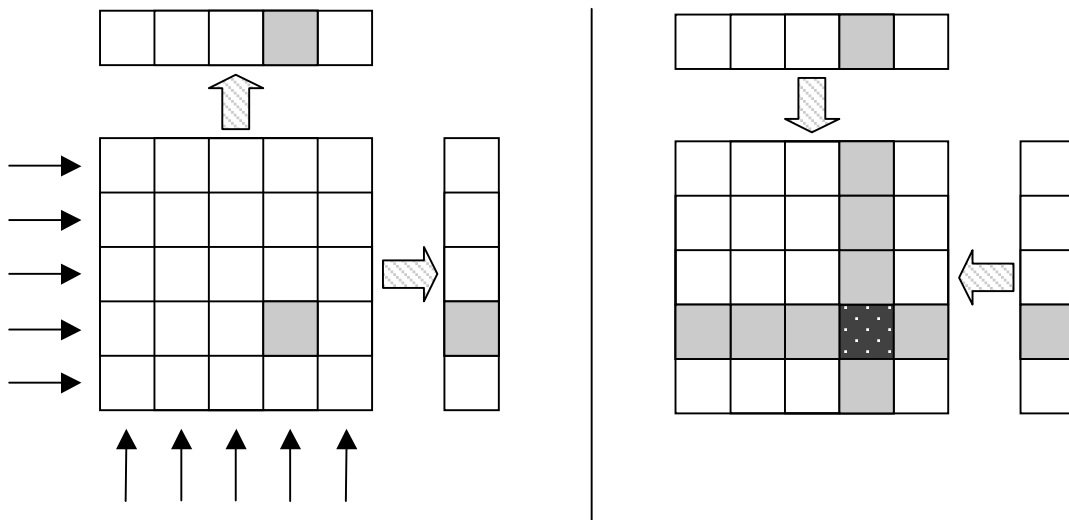
Figure 4.5. *Illustration of the backprojection process. For every rotation angle the projections are "smeared" over all pixels in the object that were transversed by the beam.*

applying appropriate mathematical functions, filters, in the transformation process and the backprojection process can be perceived as the smearing of each filtered projection over the image plane. Consequently the most widely applied method is the *filtered backprojection (FBP) algorithm*. The filter is a spatial high-pass filter that implies that the edge effects are enhanced in the reconstructed image. It compensates for the low-pass filtering effect of the backprojection process, and removes a large fraction of the star-shaped artefacts. Examples of common filters are Hann, Hamming or Ram-Lak filters. The method has been shown to be extremely accurate and amenable to fast implementation, especially since the reconstruction process can start as soon as the first projection has been taken.

It takes many projections to accurately reconstruct an object. This is demonstrated in figure 4.6, where the famous Shepp-Logan phantom has been used to simulate projection data, applying the FBP algorithm for image reconstruction. Figure 4.6 (a) shows the Shepp-Logan phantom, and figure (b), (c), (d) show reconstructions based on 19, 37 and 181 projections together with their respective sinograms. It is clear from the pictures that too few projections induce stripes and star-shaped artefacts, which are reduced with a larger number of projections. Also, note how the smoothness of the sinogram increases with the number of projections. Ideally, the number of projections should be at least $\pi N_p/2$, where N_p is the number of horizontal pixels in a projection taken at equidistant angles [58]. This ensures that there is complete data for a half revolution, with a rotation diameter of N_p, but taking projection data in all these angles is not possible in all cases.
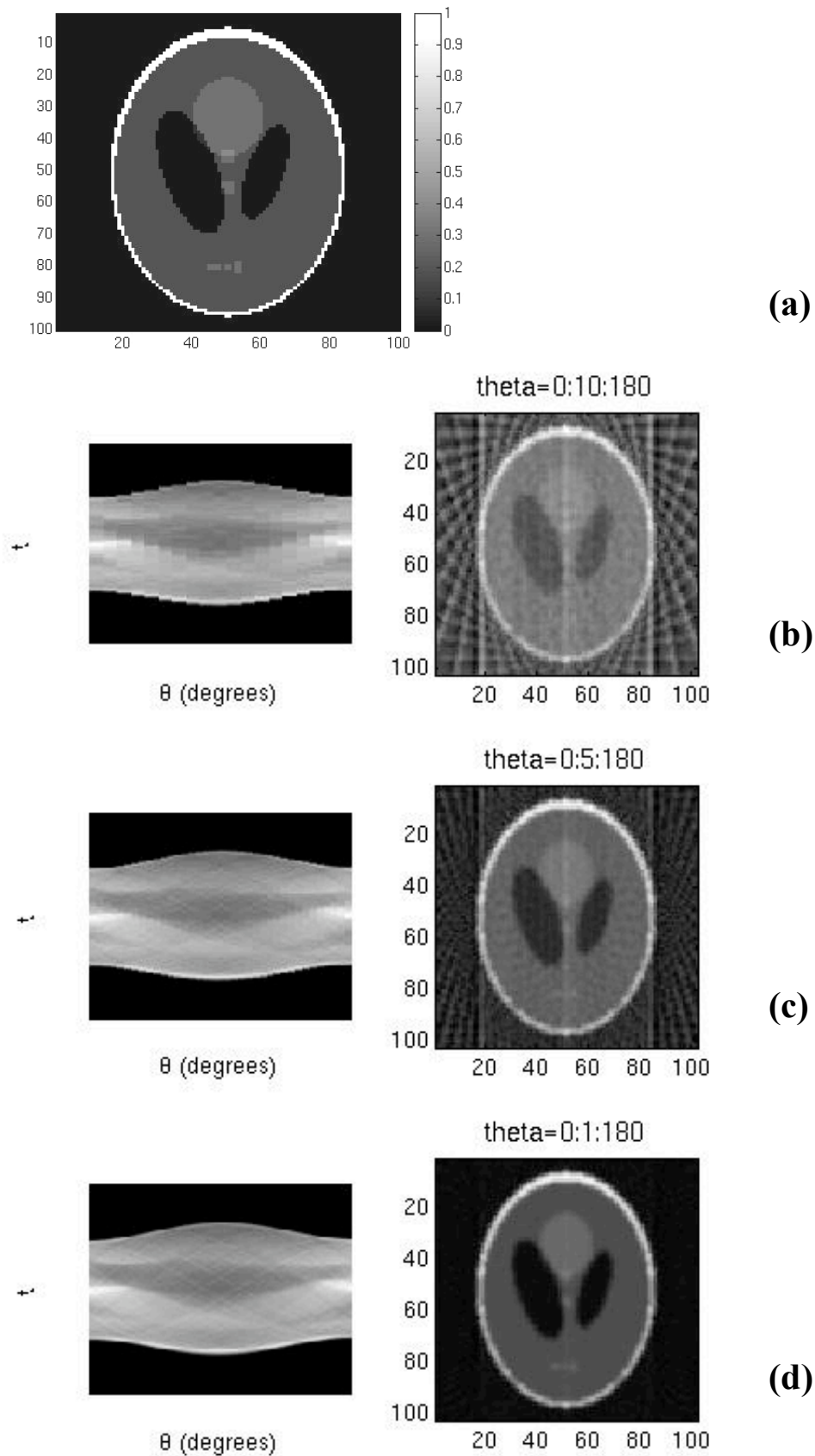
Figure 4.6. *(a) Shepp-Logan phantom, 100 × 100 pixels. (b-d) Illustration of the image quality for different numbers of projections. Reconstructions (right) and their respective sinograms (left) obtained by the filtered backprojection technique for (b) 19, (c) 37 and (d) 181 projections.*

Algebraic reconstruction techniques - ART

The most intuitive approach for tomographic reconstruction is to represent the cross section by a matrix of pixels with unknown values. The reconstruction is performed by setting up algebraic equations for the unknowns. A square grid is superimposed over the unknown image and a ray, *j*, is defined to cover the whole pixel width. The parameter value is assumed to be constant within each object pixel, and the grid lies fixed in the object as the source-detector system rotates (see figure 4.7). Another option is to assume the source-detector system to be fixed, and allow the grid to rotate with the object. Either point of view works identically and only illustrates different experimental setups. In both cases two coordinate systems have to be defined: one that is fixed and one that rotates. For every rotation angle a weigt factor, w_{jk}, has to be calculated for every pixel. This weight factor describes how large fraction of a pixel that is covered by a ray. Equation 4.8 describes how the projection value for ray *j* is determined. x_k is the value of *f(x,y)* in pixel *k*, and *M* is the total number of projections.
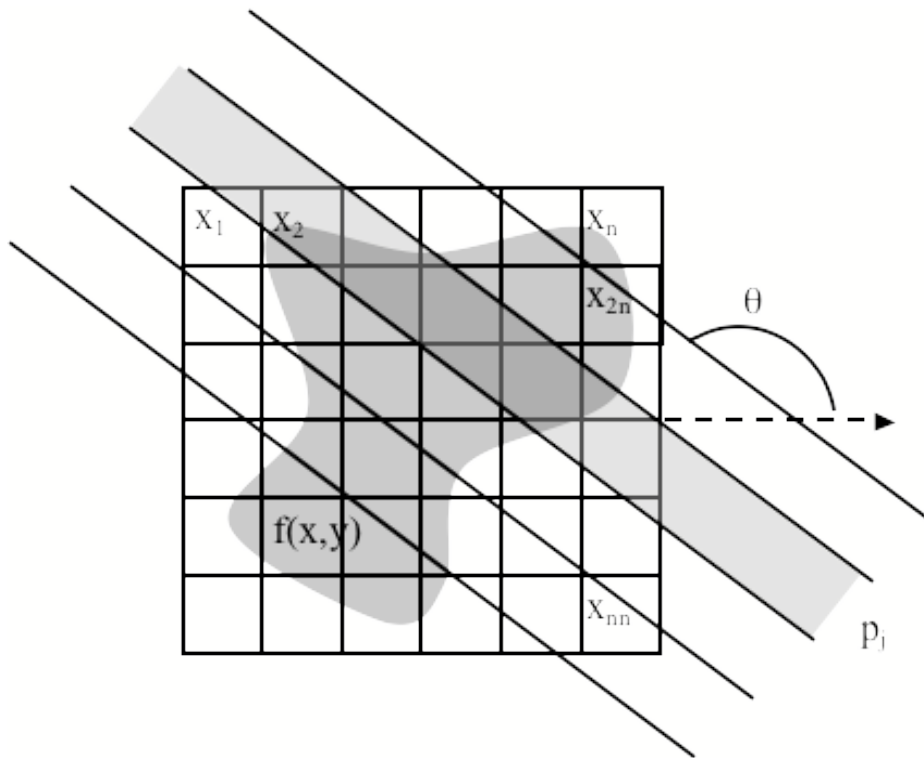
Figure 4.7. *Illustration of the geometry for algebraic reconstruction technique. The parameter value f(x,y) is assumed to be constant in every pixel and weight factors, w_{jk}, describing how much of a pixel that is covered by a ray must be determined. Freely from ref [59].*

$$p_j = \sum_{k=1}^{n \times n} w_{jk} x_k \qquad\qquad j = 1,2,...,(n \cdot M)$$

$$(4.8)$$

For a small grid and a small number of projections, conventional, direct matrix inversion can be used for image reconstruction, but this becomes impossible with noisy data, in which case some least squares method must be utilised instead. For large grids and a large number of projections, iterative methods based on Kaczmarz's

"method of projections" are popular alternatives. The principle is to make an initial guess, which is followed by a number of iterations until convergence is achieved. An example of a typical iteration process is that projection data are simulated from an estimated reconstruction matrix and are then compared to the measured projections. A correction factor is calculated and applied step by step for all object pixels that are covered by each ray. The process is repeated until a reconstruction matrix is found whose projection data reproduce the experimental values. For overdetermined systems in the presence of noise, however, there is no unique solution and hence convergence cannot be reached.

An attractive feature of the iterative approach is that *a priori* information can be included in the solution, for example zero-pixels can be identified and negative object function values can be neglected. Also physical processes can be taken into account, by introducing suitable correction factors. Algebraic methods are advantageous in situations of incomplete data (too few projections or when the projections are not evenly distributed over 180 or 360 degrees), which are requirements for accurate reconstruction with the analytical techniques described in the previous paragraph. Also a smaller number of projections are required than in backprojection techniques for an acceptable image quality. A difficulty with iterative variants is to define a criterion for when to stop the iteration process if the data are very noisy, since the noise increases with the number of iterations. For large-sized matrices, calculation and storage of the enormous number of weight coefficients becomes slow.

There are different ways of performing the corrections. In ART (*Algebraic Reconstruction Technique*) the corrections are made step-by-step along one ray at a time. SIRT (*Simultaneous Iterative Reconstruction Technique*) is similar to ART, but here the corrections are performed pixel-by-pixel taking into account the contribution from each intersecting ray. The calculation times are relatively long, and therefore algorithms based on least squares are preferred, whereby all pixels in the image are corrected simultaneously. The iterative method DISRA (*Discretised Image Space Reconstruction Algorithm*) is also worth mentioning, since over the past 10 years it has been successfully implemented by Arthur Sakellariou for ion beam tomography [58]. The mass density of inhomogeneous samples can be reconstructed very accurately with less than 10 iterations, and STIM and PIXE experiments are simulated by including physical models for ion energy loss, X-ray production cross sections and X-ray attenuation.

Statistical methods

The statistical methods rely on a probabilistic model of the reconstruction problem. The goal is to reach the most uniform image possible that is compatible with the statistical fluctuations present in the experimental data.

One example is the technique of maximum entropy, which is known to produce fewer artefacts than FBP and reduce noise. Every pixel in a backprojected image has an associated error, which is assumed to be Gaussian. The most probable map is that which maximises the entropy of the image. This is solved iteratively starting with the filtered backprojection image as the first estimate. An obvious drawback is the long image reconstruction time – typically three orders of magnitude longer than for the FBP algorithm. [60]

Another example is algorithms based on maximum-likelihood expectation maximisation (MLEM). Physical models can be directly incorporated, and it has been demonstrated that the algorithm is capable of handling highly incomplete data sets (only four projections) even in the presence of noise. Again, the computational time is considerable, with noise levels that increase with the number of iterations required to reach convergence. [61]

## 4.2 Tomography with focused ion beams at MeV energies

As discussed in a previous chapter, ions interact differently with matter than for instance X-rays, and experience both energy loss and scattering when traversing matter. This limits the range for MeV ions, often to 10-100 micrometres, depending on the initial energy, the ion mass and the target material. The range sets a limit on the maximum specimen thickness that can be analysed in transmission mode, or the maximum analytical depth of analysis in emission mode. On the other hand, the possibility to focus ion beams to micrometre and sub-micrometre size, as well as the small lateral straggling as compared to e.g. electron beams, makes them well suited for high-resolution analysis of microscopic samples such as cells, spores etc.

The use of ion beams in tomography was introduced in the mid 1980's [50,51]. Two main types have been developed, STIM and PIXE tomography, in which the mass density and element distribution, respectively, are imaged. The mass density maps are useful to image the morphology in the sample and reveal internal structures or pores. Three-dimensional mass density information can then help to perform a more correct mass density normalisation for PIXE experiments, where the usual assumption of a homogeneous element distribution over the whole sample thickness might be erroneous. To take things one step further, subsequent PIXE tomography can be performed to reach real, three-dimensional element distribution imaging and thus avoid depth-averaged quantitative data.

Other common ion beam techniques also have their tomographic equivalent, such as RBS tomography [62]. Another category of imaging techniques is focused ion beam (FIB) tomography, which is a destructive form of analysis. Sections of the sample are "milled" away to allow sample investigation with a resolution of 10 nm [63].

4.2.1 STIM tomography
In STIM tomography, the energy loss of transmitted particles is measured and transformed into areal mass density values for every projection. The reconstruction process will result in an image of the mass density distribution (in g/cm^3) in a cross section of the sample. STIM-tomography is executed with on-axis geometry to optimise the energy resolution, and the energy and ion species is adjusted for optimal contrast in the object in question. The minimum acceptable residual energy is set above the Bragg peak where the energy loss is dominated by electron stopping. In reality it is difficult to optimise the beam energy to the specific sample thickness, since this parameter is not always known beforehand. A typical experimental setup is illustrated in figure 4.8.
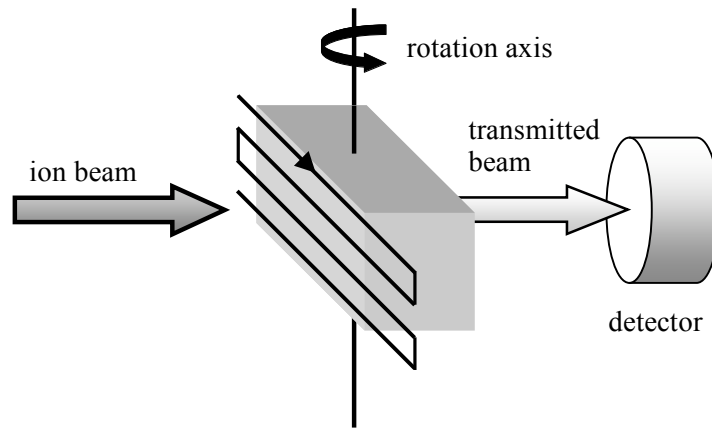
Figure 4.8. *Illustration of the geometry for STIM tomography*

In every ion beam experiment it is important to deliver as small a dose as possible to the specimen, to avoid shrinking effects due to heating, redistribution of volatile elements etc. Here STIM tomography is a suitable candidate for fragile samples since, despite the long irradiation times required, the current conditions in place guarantee minimum sample damage.

4.2.2 PIXE tomography

In PIXE-tomography, the characteristic X-ray emission is detected as the sample is rotated through a number of angles. X-rays are attenuated as they travel through material, and by estimating the degree of attenuation in the sample matrix, the position of the emission point, i.e. the place where the beam ion interacted with the target element, can be located. The major constituents of the sample matrix must be known in advance, for example via a previous standard PIXE or RBS experiment. Also the mass density distribution should be known, for instance from a STIM tomography experiment. Since the degree of X-ray attenuation is dependent on the path through the sample, the projections must be acquired over a full 360° rotation, compared to 180° for a STIM data set.

PIXE tomography is most commonly performed for minor and major elements, but the quantification can be performed only with an accuracy close to 10% if the sample contains low-Z elements, which cannot be detected with PIXE [2,64]. For trace element tomography [61] the mass density and mass fraction distributions must be known in advance, for example from a normal PIXE tomography experiment, and the distributions can be reconstructed by performing small corrections to the *a priori* known major-minor element compositon.

A PIXE tomography experiment is much more time consuming than the STIM equivalent. The energy spectra must contain sufficient statistics for every element whose distribution is to be reconstructed. Another essential difference between STIM and PIXE is that virtually every ion in the beam is detected in STIM, but in PIXE the majority of ions do not contribute to the detected X-rays [65]. Therefore the beam current has to be much higher than for STIM conditions, and consequently the beam size is larger. Still, the analytical time is very long and there is more risk of beam-induced sample damage. For this reason, a large-area HPGe detector has been installed in the experiment chamber at the Lund sub-micron

beamline. The detector is positioned in the backward direction and consists of 8 separate elements, with a total area of 8×100 mm^2, positioned in a circle around a hole for beam passage. With this large detector area, the time required to obtain the desired statistics is reduced many times compared to that needed for one standard detector element.

The large-area detector has still not been satisfactorily calibrated, and the data reconstruction technique is so far only dedicated to STIM tomography, and will be further described in the following paragraphs. No further description of physical phenomena to be considered in the reconstruction of PIXE data will be given here. Future developments, however, include an expansion of the tomographical examination to involve PIXE tomography for samples for which such information could be of importance. This is further commented on in section 4.5.


4.3 The Lund tomography system

For tomography experiments, the ordinary sample holder is replaced by a sample manipulator attached to a "DC-Motor-Gearhead" drive-unit (Model C136-10 from Physik Instrumente (PI)) [66]. The manipulator is attached to a stage, which can be manually tilted by adjusting a ball pivot, and this stage is mounted on the standard X-Y-Z sample stage. A tungsten needle with a 0.6 μm radius at its tip is used as the rotation axis and the rotation motor is capable of rotation in steps of 0.0068°. The stage on which the sample manipulator is mounted, also holds a rod with a calibration grid attached to a quartz plate (see figure 4.9). This assembly is utilised for focusing the beam and for determining the size of the beam spot.

The STIM detector is a windowless Hamamatsu p-i-n diode (S1223, 4×4 mm), which is mounted in on-axis geometry on the moveable stage for the rear microscope in the experiment chamber. This allows for small movements in the X-direction in the detector position, to avoid local detector damage during the experiment.

The manipulation of the rotation axis is controlled by the data acquisition system, where the angles are retrieved from a user-defined list. In order to guarantee equidistant projection data, covering the whole 180° angle interval even in case of a premature abortion of the experiment, the angles are not chosen in sequential order. Instead they are taken in different series, with decreasing distance, filling out the empty spaces between the projection angles from the previous series.

A sample of suitable dimensions is prepared and glued to the tip of the tungsten needle with carbon glue. This is very difficult, since no micromanipulators are available, and it has to be executed by hand with tweezers and scalpels under an ordinary optical microscope. The small samples are very fragile, and it takes several attempts to fixate them in a good position on the needle without breaking, bending or loosing the sample by an air current.
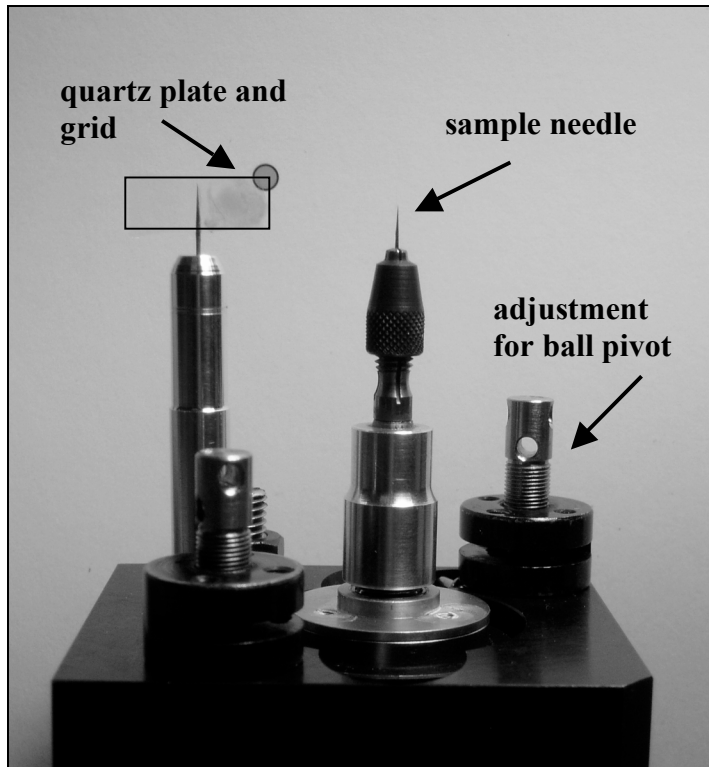
Figure 4.9. *Setup for sample manipulation including a copper grid and a quartz plate for beam focusing.*

The alignment of the rotation axis has to be performed in air. The sample is viewed in the rear microscope as it is rotated, and the pitch screws for the ball pivot are adjusted until the sample rotates nicely around a vertical axis. Unfortunately, no matter how good it looks in air, the alignment is subject to changes when the chamber is closed and pumped for vacuum.

4.3.1 The STIM tomography experiment

The ion beam is focused according to standard procedures, after which the beam current is decreased towards STIM conditions by closing the object slit step-by-step. The STIM detector is positioned slightly off-axis, in order not to damage it by beam-currents which are too high. The detector is slowly moved closer to its on-axis position, while the object opening is further decreased so that the detector count rate from a calibration sample remains below 10 kHz. The on-axis position is confirmed by letting the beam pass a hole in the calibration sample. When the beam is off-axis, ions reach the detector via scattering in the calibration sample, but no scattering can occur in a region with a hole. In the on-axis position, straight propagating ions can reach the detector, without relying on scattering in a sample, and hence the incident ion energy can be measured with the detector. Figure 4.10 (b) shows a typical calibration foil of two crossed Mylar foils of different thickness and a hole area. Figure (a) shows the corresponding spectrum for the residual energies corresponding to the four different thicknesses represented in (b). This kind of calibration sample is used for energy calibration in combination with tabulated stopping power information for the material, or simply for surface density calibration.
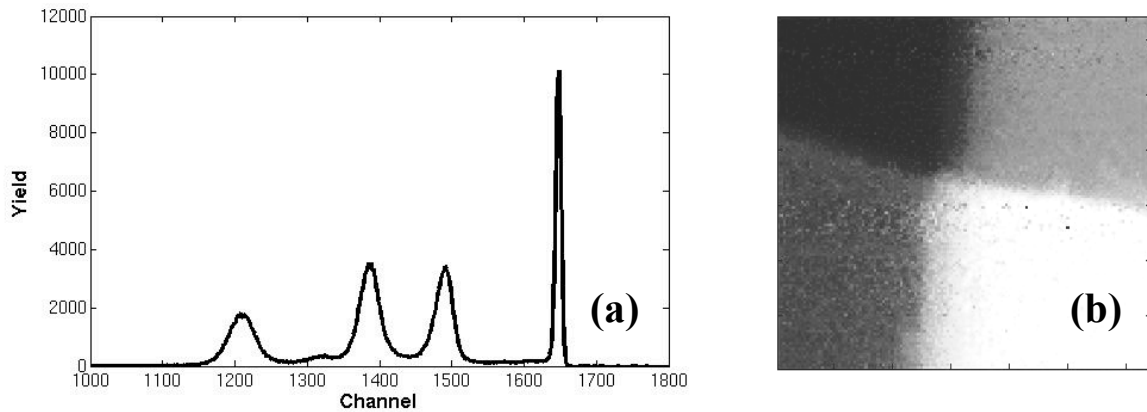
Figure 4.10. *(a) Residual energy spectrum for a calibration sample consisting of two crossed Mylar foils, 12 and 23 µm, respectively. (b) Corresponding STIM map. The upper left region (hole) corresponds to the peak at channel 1650, which represents the incident ion energy. The other three regions represent the peaks in figure (a) for 12, 23 and 35 µm Mylar thickness.*

A number of ions are detected in every pixel as the beam is scanned over the sample. To present the residual energy in a two-dimensional map, the average or median energy value of the ions detected in every pixel is calculated. Both methods are advantageous in different situations. Taking the median value requires fewer detected ions per pixel for a representative value than with average value filtering, and offers sharp resolution as well as lower noise levels [67-70]. Average filtering is, on the other hand, generally better in resolving small structures, even with sub-beam resolution for features of highly varying density [71], which is important in the application discussed in section 4.4.1, why exclusively this kind of filtering has been utilised in this thesis work.

Energies that apparently do not originate from a transmitted ion, and hence would strongly impair the average value, are eliminated by introducing an energy window in the energy spectrum, into which a detected ion has to fit in order to be accepted. Examples of false events that can reach the detector, but can be eliminated with the energy window, originate from slit scattering, pulse pile up etc [72].

Each projection was acquired with a count rate of less than 10,000 ions per second and a scanning frequency of 250-1000 Hz. The image was scanned twice if zero-pixels appeared in the image. The scan region was selected to cover the tip of the sample, to always have a reference point in the image whose y-position should be constant in the case of perfect precession around a vertically aligned rotation axis. Small deviations from the ideal rotation may be corrected for off-line with dedicated software. Ideally,
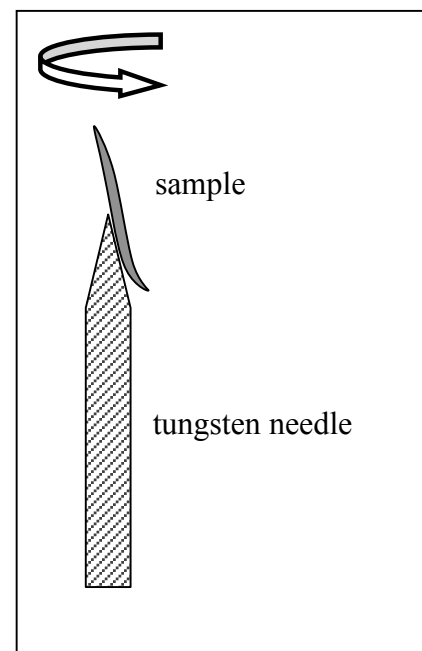
Figure 4.11. *Sample mounting on tungsten needle.*

the sample should be mounted on top of the needle, symmetrically on the rotation axis, but since this is very difficult to achieve with the crude sample mounting technique described earlier, the sample often ends up glued flat to one of the sides of the tip of the needle (see figure 4.11). To save time and avoid scanning over the majority of zero-value pixels outside the sample, the scan region is selected reasonably tightly around the sample, and is allowed to follow the sample as it rotates.

As a rule of thumb, one ray should be utilised per resolution element and the ideal number of projections is $(\pi/2)N_p$, where N_p is the number of horizontal pixels in a projection. [58,72]

## 4.3.2 Data analysis and reconstruction technique with examples

The projection data can be stored either as event files for later processing or as two-dimensional STIM maps. The STIM maps display the energy difference between a preset maximum energy, typically the incident ion energy, and the average residual energy in every pixel. All projection data are tagged with the corresponding rotation angle. The STIM maps are converted to areal mass density maps with the use of the mass densities that are known from the calibration sample, or by the use of stopping power data for a known sample composition assuming that the sample is homogeneous.

The filtered backprojection algorithm was chosen for the reconstruction, since it is known to be fast, easy to implement and able to produce images of good quality. The density information achieved by a STIM experiment is identical to the addition of the mass density values along the beam path for each projection, "normalised" to the voxel dimension. For this reason a backprojection algorithm can be utilised to determine volume density values (g/cm^3) from surface density values (g/cm^2). The algorithm is realised in MatLab, using predefined functions (e.g. "iradon") from the image processing toolbox for the purpose. Before applying the filtered backprojection algorithm, data are corrected and adjusted with an in-house-written computer code for improper alignment, for identifying and adjusting the rotation axis and for identifying zero-pixels. The principle for adjusting the rotation axis has been described by Azevedo et al. [73]. The inverse Radon transform is implemented for every horizontal line in the projection data set, with a free choice of filter, interpolation method and frequency cut-off as seen in table 4.1. The filter is designed directly in the frequency domain, and the projections are zero-padded before filtering to prevent spatial domain aliasing and to speed up the fast Fourier transform [74].

Table 4.1. *Possible choices for the implementation of the filtered backprojection algorithm in Matlab with the "iradon" function.*

Filter	Interpolation method	Frequency cut-off
Hann	Nearest neighbour	0.0 – 1.0
Hamming	Linear	
Shepp-Logan	Spline	
Cosine		
Ram-Lak		

Applying a frequency cut-off resulted in smoothing the image, which decreased the noise level, but turned out to be highly unsuitable for the identification of small structures in the reconstructed image. Figure 4.12 shows the effect of a 60% frequency cut-off in the reconstruction of a cross section of a glass micro-capillary.
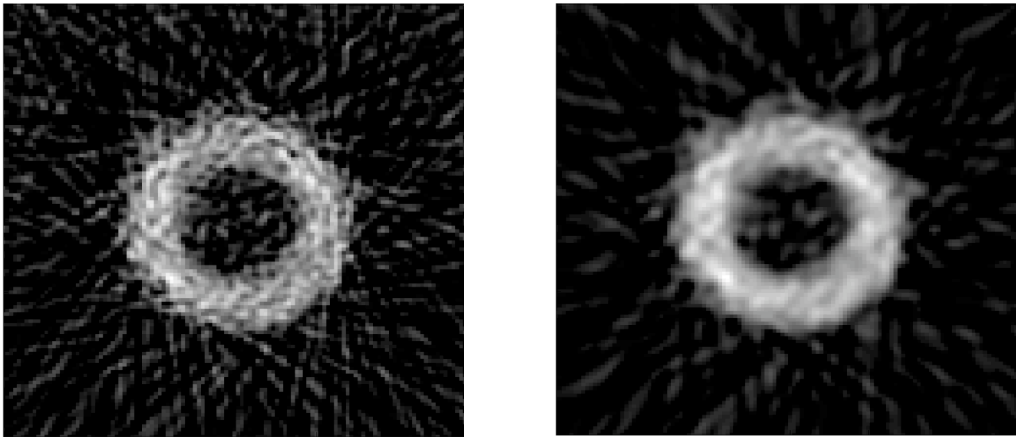
Figure 4.12. *Reconstructed cross-section of a glass micro-capillary (120×120 pixels, 0.4 μm step size), with a 60% frequency cut-off for the image to the right. Both images have been reconstructed from 46 projections with a filtered backprojection algorithm (Hann filter).*

If the reconstructions for each horizontal line in the projection data set are stacked, the full three-dimensional information is gathered and can be displayed in different ways. The sample morphology can be illustrated by selecting a mass density value to produce an iso-surface, such as in figure 4.13, or equidistant cross sections can be presented, as in figure 4.14. A cut can be realised at any position in the sample to reveal the internal structure. With special volume-rendering software, outer contours and layers of the sample can be made transparent to mediate the visualisation of internal structures of a defined mass density.
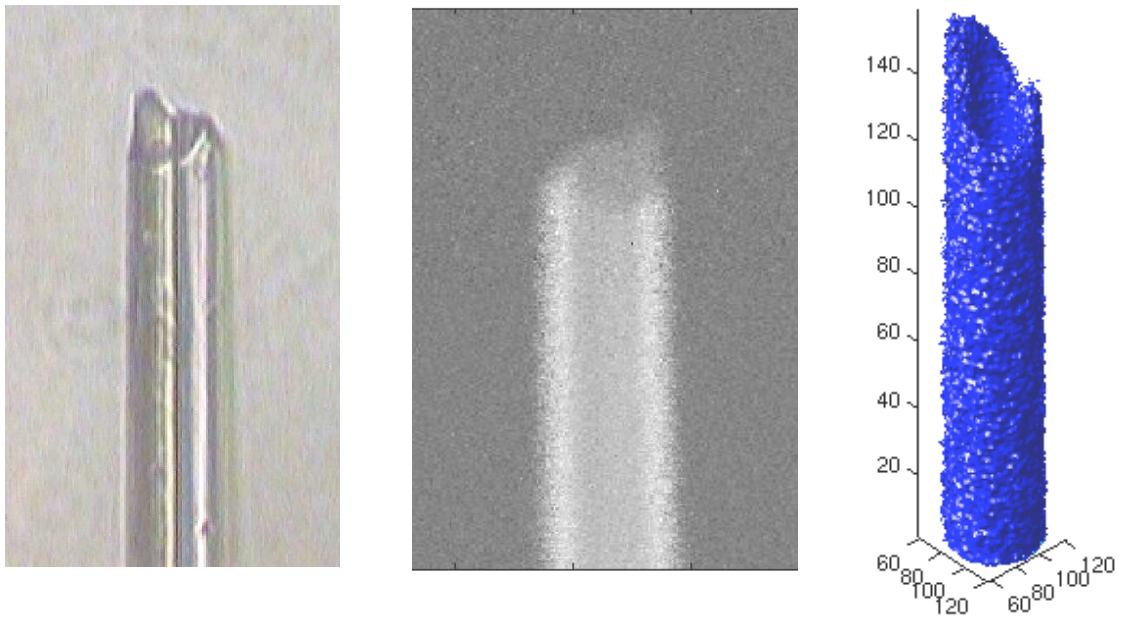
Figure 4.13. *Photo of a glass micro-capillary with an outer diameter of approximately 25 μm (left), a STIM projection map (middle) and the reconstructed image (right) displaying iso-surface values for illustration of the sample morphology.*
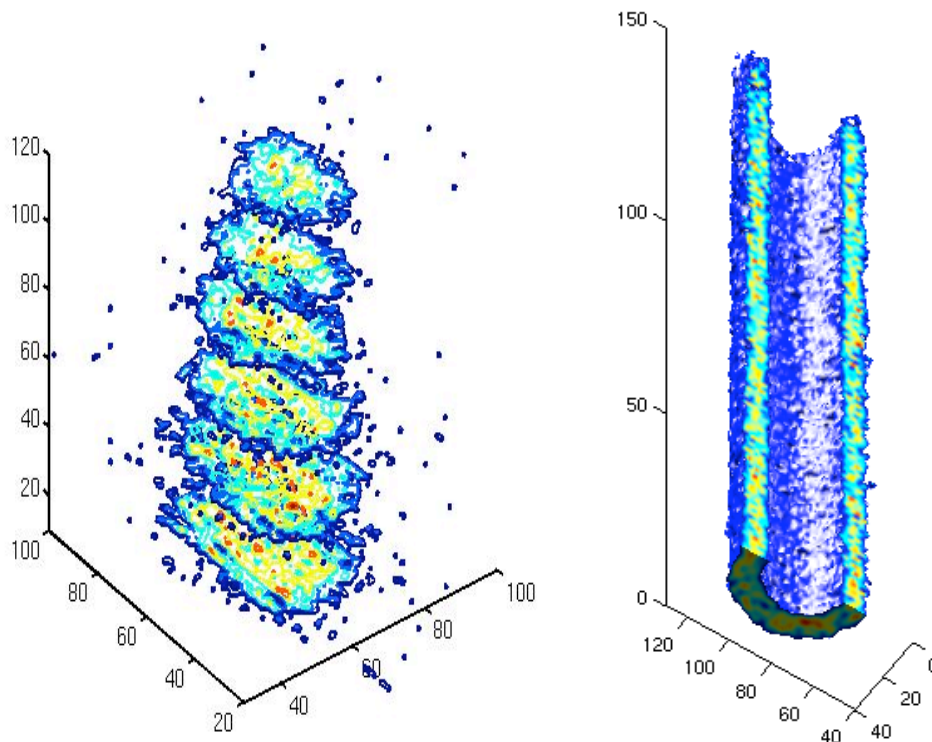
Figure 4.14. *Stacked, equidistant cross sections of a bentonite clay sample (left) and an iso-surface image combined with a cut through a glass micro-capillary for illustration of both the morphology and internal structure of the sample (right).*

4.4 Applications of microtomography

Microtomography with ion beams opens up possibilities for non-invasive, high-resolution imaging of morphology, internal structures and three-dimensional element distributions in a sample. Depending on the conditions for the analysis, e.g. beam-current, the tomographic investigation can be almost totally non-destructive. There are vast application areas, in disciplines like biology, geology, environmental science, material science etc. Some examples of are investigations on cells, spores, element distributions in a scorpion stinger and pollen [67,68,75,76]. The Lund tomography setup has been used for the analysis of porosity in bentonite clay, as described in more detail in section 4.4.1, but is also aimed for other applications, such as in paper physics to study ink penetration and porosity, as well as in analysis of single aerosol particles.

4.4.1 Porosity studies in bentonite clay

Bentonite clay is planned to be used in the KBS-3 [77] concept for a future nuclear high level waste (HLW) repository in Sweden. In the concept the spent nuclear fuel is placed in and iron insert, which is encapsulated in a copper canister using friction stir welding (FSW). The copper canister is embedded in compacted bentonite and deposited at 500 m depth in granite bedrock. The compacted bentonite will act as a buffer material, giving mechanical support for the copper canister, reducing water movements and capturing potentially escaping radionuclides.

Bentonite is a natural clay, which has a high swelling capacity in water, originating from its high content of smectite minerals. Smectite minerals, with montmorillonite as the most common, are sheet silicates, which can intercalate water into their structure by hydrating interlayer cations. This causes expansion of the interlayer distances and an exceptional swelling capacity, which makes bentonite a suitable buffer material that works as a sealant and barrier [78]. The hydration process is reversible, and in a dry atmosphere or during heating, both water and hydrated cations can leave the structure of montmorillonite [79].

Heterogeneity in the material, compaction and in swelling may result in porosity, both on the nano- and micrometre scale, which may affect the permeability of the clay and may mediate the transport of radionuclides, cations and corrosion products. In a porous mineral structure, the swelling will reduce the pore volume until the original pore volume is filled with water, i.e. full water saturation [80]. Water can continue to move in order to balance the interlayer ion concentration in the system, and any remaining differences in ion concentrations lead to an osmotic pressure, which can separate the layers up to 10 nm. The density of the bentonite determines the amount of free pore water. At high density, e.g. at high outer pressure, the largest fraction of the water is bound, and the structure will be a better sealant [81]. The final pore-size distribution determines the hydraulic permeability and governs the possible transport of colloids, and material transport by advective flow. Hence, also the thermal gradient around a copper canister of decaying fuel will contribute to a redistribution of water [82]. Investigations in combination with simulations have resulted in an estimation that the bentonite buffer surrounding a copper canister with decaying nuclear fuel, will be fully water saturated after 3-4 years, provided that there is access to water [83].

Ion beam analysis was applied in order to investigate the mineral composition and pore distribution in bentonite. The pore size normally ranges from nano- to micrometre size, which makes ion beam analysis suitable mainly for the larger pores. The analytical techniques used were scanning transmission ion microscopy (STIM), particle-induced X-ray emission (PIXE) and elastic p-p scattering. PIXE analysis was performed in order to investigate the element distribution in the samples, and hydrogen analysis was performed with the elastic p-p scattering technique, in order to measure the water content, i.e. the degree of saturation, in the sample. On-axis STIM analysis was performed in tomographic mode in order to measure and map the mass density of the sample in the search for pores.

The bentonite samples were prepared according to a procedure described thoroughly in paper IV and briefly in chapter 3.3.1, where the clay was dissolved in water and dried to a thin film on a supporting Mylar foil. For tomography, thin strips were cut from the bentonite film, with dimensions suitable for analysis in transmission geometry.

The effect of beam straggling was evaluated with SRIM simulations. A 2.55 MeV proton beam passing through a benonite matrix of 12 μm respective 18 μm thickness, experiences a lateral straggling of 0.16 μm respective 0.36 μm (FWHM). With a beam spot size of approximately 1 μm, beam straggling is not considered to seriously deteriorate the spatial resolution.

In order to maintain as much information in the image as possible, and avoid deterioration of the resolution by smoothening processes, very little image processing was performed. No frequency cut-off was applied in the filtered backprojection process. The tomographic reconstruction showed that the bentonite had an interesting internal structure, with micrometre-sized features indicating both accessory minerals and possible pores. This can be observed in figure 4.14 (left) and in figure 4.15.
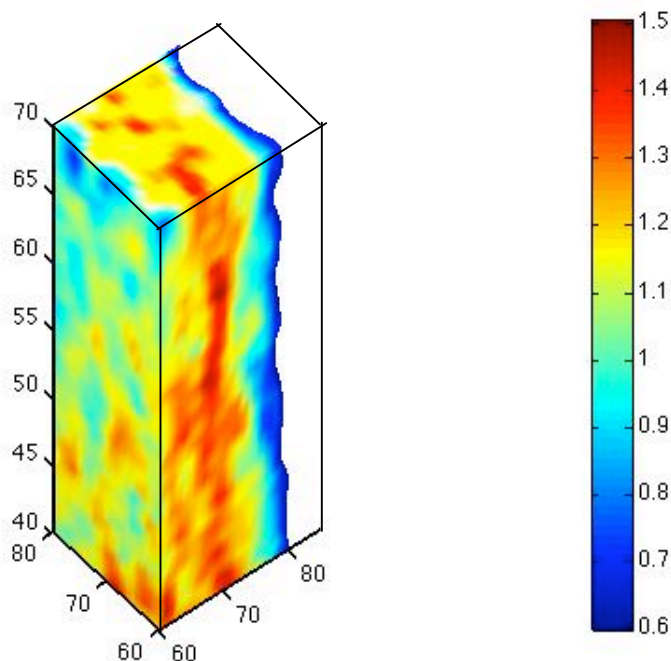
Figure 4.15. *Internal structure of bentonite sample (12×12×18 μm³). Colourbar showing mass density (g/cm³).*

A more common method for porosity studies is *Mercury Intrusion Porosimetry*, where mercury is forced to penetrate into the sample, which is weighed before and after treatment. The pressure required for the penetration is a function of the pore size, but reveals nothing about the spatial distribution of the pores. However, combining the mercury treatment with standard PIXE analysis could be an interesting alternative to pore identification through mass density measurements (in 2D or 3D mode).

A beautiful work worth mentioning is a study of aging and porosity development in cement pastes, with synchrotron X-ray tomography [84]. Using X-rays instead of ions, allows for larger samples and with the use of a CCD camera, there is no need for beam focusing or scanning, and consequently an image can be acquired with a very short exposure time (3 s per projection). This makes a tomographic investigation reasonable when it comes to the time needed for data acquisition. The resolution was limited by the similar attenuation coefficients of pores and hydrated cement relative to unreacted cement. Interesting information can possibly be obtained with a combination of phase and absorption contrast, which has become "popular" with the 3rd generation synchrotron light sources [52].

4.5 Outlook

A tomography system has been designed and implemented at the Lund Nuclear Microprobe. The development has passed the initial state, and successful experiments have been performed both for testing the system and for real applications. Several factors can still be improved for more accurate quantitative STIM tomography investigations. Access to the well-established DISRA software, especially developed for STIM and PIXE tomography, will facilitate data reconstructions in the future with which more physical phenomena are modelled and considered. The DISRA code can also be expanded to be able to handle PIXE tomography data from the 8-element HPGe-detector.

At the moment, the data acquisition and rotation control is not fully automated. With a more automated system, data acquisition becomes less demanding for the experimentalist and more projection angles can be investigated within shorter time-spans. The beam scanning should be controlled by the number of detected ions per pixel, instead of by a fixed scanning frequency, to make the most of the time spent for irradiation. A PIXE experiment would also benefit from this modification, since it would allow the X-ray yield to be normalised with respect to the charge in every pixel.

Correct alignment of the rotation axis proved to be of utmost importance. Although small misalignment can be manually corrected for in the projection data set, the ball pivot stage holding the rotation motor should be replaced with a type that can be manipulated in vacuum from outside the chamber. Also the sample mounting technique should be improved. One idea is to utilise a microcapillary as rotation axis and sample holder, where the sample can be mounted either on top of the capillary tip or be inserted into the capillary. This could be an interesting method for enclosing bentonite slurry for more extensive porosity studies.

Acknowledgments

Many people have helped and supported me during the years of my PhD studies. Without you it would have been impossible to finish this work, and my time at the Division of Nuclear Physics in Lund would most definitely have been a lot less fun. Here I would like to express my sincere gratitude and warmest thanks to you all, starting with:

- my outstanding supervisor Professor Per Kristiansson. Thank you for always having your door open to me, and for giving your time for guidance, discussions and helping me out in the lab. I am especially grateful for the confidence you have shown me, and the freedom you have given me to work independently. Also I have enjoyed so much working with pulse electronics, learning how to run the accelerator and to align the ion beam optics – all in your company.

- Dr. Mikael Elfman, who has been a dear friend and given me an enormous amount of help and support, no matter what my problem was. I have enjoyed our discussions and working side by side with you in the lab all these evenings and late hours.

- my other colleagues in the micro group: Jan Pallon and Christer Nilsson, thank you for being friendly, helpful and teaching me practical things in the accelerator lab.

- my fellow PhD students and great friends in the micro group – both past and present: Charlotta Nilsson, Natalia Arteaga Marrero, Vaida Auzelyte and Asad Shariff. I will always remember and value highly the good times we have had together at work, at conferences and in our spare time.

- past and present room mates: especially Dr. Adam Kristensson and Master's students Joanna Boquist and Jeppa Resmark. You have been great company!

- all the rest of my colleagues at the Division of Nuclear Physics. Together we have created a warm and friendly working environment.

- my collaborator and co-author Henrik Skogby at NRM in Stockholm is also thanked, together with his PhD student Rickard Sundvall, for providing me with samples for the hydrogen analysis, for explaining things about geology and mineralogy and for visiting me in the lab.

- my collaborators and co-authors PhD student Daniel Svensson and Dr. Anders Sjöland from SKB (Swedish Nuclear Fuel and Waste Management Co) who provided me with the bentonite samples.

- and finally my family and friends outside work. Thank you for encouraging me at all times. A special thank you to my parents, Margaretha and Ingvar, who have proudly supported me during all my years at school and encouraged me to get a solid education. Thank you also to my brother Henrik, who has shown me care, love and great friendship.

My warmest thanks go to my dear Fredrik, for his love, constant support and care of our home. Thank you also for your patience and for coping with my late evenings during accelerator runs, especially during the final months of my studies.

E finalemente… Da due anni studio l'italiano una volta alla settimana. Mi è piaciuto fare e pensare a qualcos'altro della fisica ed il mio lavoro con questa tesi. Ma, per arrivare alla lezione in tempo, sono dovuta andarmene più prima del solito dal mio lavoro. Per Kristiansson, il mio istruttore, mi ha detto per scherzo che ha soltanto potuto permettermi andare più prima dal lavoro, a condizione che io scrivessi una parte della mia tesi in italiano. Cioè questa piccola parte che ho scelto di scrivere qui…

Tanti saluti e grazie mille a tutti,

Marie

References

1. U.A.S Tapper and K.G. Malmqvist, *Analysis, imaging, and modification of microscopic specimens with accelerator beams*, Analytical Chemistry, 1991, 63, 715 A-725 A.
2. A. Sakellariou, Doctoral thesis, *STIM and PIXE Tomography, The Three-Dimensional Quantitative Visualisation of Micro-Specimen Density and Composition*, University of Melbourne, 2004.
3. J.R. Tesmer, M. Nastasi, *Handbook of modern ion beam materials analysis*, Materials Research Society, 1995.
4. S.A.E. Johansson, J.L. Campbell, K.G. Malmqvist, *Particle-Induced X-ray Emission Spectrometry (PIXE)*, John Wiley and Sons Ltd, New York, 1995.
5. G.W. Grime, F. Watt, *Beam Optics of Quadrupole Probe-Forming Systems*, Adam Hilger, Bristol, 1994.
6. Kenji Kimura, Kaoro Nakajima, Hideki Imura, *Hydrogen depth profiling with sub-nm resolution in high-resolution ERD*, Nucl. Instr. and Meth. B 140 (1998) 397-401.
7. J. Pallon, V. Auzelyte, M. Elfman, M. Garmer, P. Kristiansson, K. Malmqvist, C. Nilsson, A. Shariff, M. Wegdén, *An off-axis STIM procedure for precise mass determination and imaging*, Nucl. Instr. and Meth. B 219-220 (2004) 988-993.
8. Vaida Auzelyte, Doctoral thesis, *Direct Writing with an MeV Proton Beam: Development and Applications*, Lund Institute of Technology, Lund University, 2006.
9. Vaida Auzelyte, Mikael Elfman, Per Kristiansson, Klas Malmqvist, Lars Wallman, Christer Nilsson, Jan Pallon, Asad Shariff and Marie Wegdén, *The beam blanking system for microlithography at Lund Nuclear Microprobe*, Nucl. Instr. and Meth. B 219-220 (2004) 485-489.
10. V. Auzelyte, M. Elfman, P. Kristiansson, J. Pallon, M. Wegdén, C. Nilsson, K. Malmqvist, B.L. Doyle, P. Rossi, S.J. Hearne, et al., *Fabrication of phosphor micro-grids using proton beam lithography*, Nucl. Instr. and Meth. B 242 (2006) 253-256.
11. A. Ressine, V. Auzelyte, P. Kristiansson, G. Marko-Varga, T. Laurell, *Fabrication of sample target plate for MALDI MS using proton beam writing*, Nucl. Instr. and Meth. B 249 (2006) 715-718.
12. Vaida Auzelyte, Mikael Elfman, Per Kristiansson, Christer Nilsson, Jan Pallon, Natalia Arteaga Marrero and Marie Wegdén, *Exposure parameters for MeV proton beam writing on SU-8*, Microelectronic Engineering 83 (2006) 2015-2020.
13. N. Arteaga-Marrero, J. Pallon, M.G. Olsson, V. Auzelyte, M. Elfman, P. Kristiansson, K. Malmqvist, C. Nilsson and M. Wegdén: *The new Cell Irradiation Facility at the Lund Nuclear Probe*, Nucl. Instr. and Meth. B 260 (2007) 91-96.
14. Charlotta Nilsson, Jan Pallon, Göran Thungström, Natalia Arteaga, Vaida Auzelyte, Mikael Elfman, Per Kristiansson, Christer Nilsson and Marie Wegdén: *Evaluation of a pre-cell hit detector for the future single ion hit facility in Lund*, Nucl. Instr. and Meth. B 249 (2006) 924-927.
15. N. Arteaga-Marrero, V. Auzelyte, M.G. Olsson and J. Pallon, *A SU-8 dish for cell irradiation*, doi:10.1016/j.nimb.2007.06.012
16. A. Shariff, Doctoral thesis, *Development of New Experimental Facilities at the Lund Nuclear Microprobe Laboratory*, Lund Institute of Technology, Lund University, 2004.

17. A. Shariff, K. Bülow, M. Elfman, P. Kristiansson, K. Malmqvist, J. Pallon, *Calibration of a new chamber using GUPIX software package for PIXE analysis*, Nucl. Instr. and Meth. B 189 (2002) 131-137.

18. Asad Shariff, Vaida Auzelyte, Mikael Elfman, Per Kristiansson, Klas Malmqvist, Christer Nilsson, Jan Pallon and Marie Wegdén, *The Lund Nuclear Microprobe sub-micron set-up. Part I: Ion optics calculation*, Nucl. Instr. and Meth. B 231 (2005) 1-6.

19. Asad Shariff, Per Kristiansson, Vaida Auzelyte, Mikael Elfman, Klas G. Malmqvist, Christer Nilsson, Jan Pallon and Marie Wegdén, *Characterization of a new large area HPGe X-ray detector for low beam current application*, Nucl. Instr. and Meth. B 219-220 (2004) 494-498.

20. V. Auzelyte, F. Andersson, M. Elfman, P. Kristiansson, J. Pallon, M. Wegdén, C. Nilsson and N. Arteaga Marrero, *On-line measurement of proton beam current in pA range,* Nucl. Instr. and Meth. B 249 (2006) 760-763.

21. Mikael Elfman, Per Kristiansson, Klas Malmqvist, Jan Pallon, Anders Sjöland, Rogerio Utui, Changyi Yang, *New CAMAC based data acquisition and beam control system for Lund nuclear microprobe*, Nucl. Instr. and Meth. B 130 (1997) 123-126.

22. Mikael Elfman, Per Kristiansson, Klas Malmqvist, Jan Pallon, *The layout and performance of the Lund nuclear microprobe trigger and data acquisition system*, Nucl. Instr. and Meth. B 158 (1999) 141-145.

23. Hikaru Iwamori, *Transportation of H_2O beneath the Japan arcs and its implications for global water circulation*, Chemical Geology 239 (2007) 182-198.

24. Patrick Reichart, Doctoral thesis, *Dreidimensionale Wasserstoffmikroskopie mittels Proton-Proton Streung*, Technische Universität München, 2004.

25. P. Berger, J.-P. Gallien, H. Khodja, L. Daudin, M.-H. Berger and A. Sayir, *Hydrogen incorporation into high temperature protonic conductors: Nuclear microprobe microanalysis by means of $^1H(p,p)^1H$ scattering*, Nucl. Instr. and Meth. B 249 (2006) 527-531.

26. H. Skogby, *Mineral synthesis by flux growth methods*, NATO Adv. Sci. Instr. Ser. C, Math. Phys. Sci. 543 (1999) 509.

27. P. Reichart, G. Dollinger, A. Bergmaier, G. Datzmann, A. Hauptner, H. -J. Körner and R. Krücken, *3D hydrogen microscopy with sub-ppm detection limit*, Nucl. Instr. and Meth. B 219-220 (2004) 980-987.

28. B.L. Cohen, C.L. Fink and J.H. Degnan, *Nondestructive Analysis for Trace Amounts of Hydrogen*, J. Appl. Phys. 43 (1972) 19.

29. J.F. Ziegler et. al., *Profiling hydrogen in materials using ion beams*, Nucl. Instr. and Meth. 149 (1978) 19-39.

30. M. Wegdén, P. Kristiansson, H. Skogby, V. Auzelyte, M. Elfman, K.G. Malmqvist, C. Nilsson, J. Pallon, A. Shariff, *Hydrogen depth profiling by p-p scattering in nominally anhydrous minerals*, Nucl. Instr. and Meth. B 231 (2005) 524-529.

31. K. Furuno, T. Komatsubara, K. Sasa, H. Oshima, Y. Yamato, S. Ishii, H. Kimura and M. Kurosawa, *Measurement of hydrogen concentration in thick mineral or rock samples*, Nucl. Instr. and Meth. B 210 (2003) 459-463.

32. Bengt G. Martinsson and Per Kristiansson, *A high-sensitivity method for hydrogen analysis in thin targets*, Nucl. Instr. and Meth. B 82 (1993) 589-599.

33. K.A. Sjöland, P. Kristiansson, M. Elfman, K.G. Malmqvist, J. Pallon, R.J. Utui, C. Yang, *A new detector for hydrogen analysis with a nuclear microprobe,* Nucl. Instr and Meth. B 124 (1997) 639.

34. W.A. Lanford, *Analysis for hydrogen by NRA and ERD*, Nucl. Instr. and Meth. B 66 (1992) 65.

35. H. Enge, *Introduction to nuclear physics*, Addison-Wesley, Massachusetts, 1970.

36. D.J. Knecht, S. Messelt, E.D. Berners, L.C. Northcliffe, *Proton-Proton Scattering from 1.4 to 2.4 Mev*, Phys. Rev. 114 (1959) 550.
37. Jorge. Tirira, Yves Serruys and Patrick Trocellier, *Forward Recoil Spectrometry: Applications to Hydrogen Determination in Solids*, Plenum Press, New York, 1996, ISBN 0-306-45249-9.
38. P. Reichart, G. Dollinger, A. Bergmaier, G. Datzmann, A. Hauptner, H-J. Körner, *Sensitive 3D hydrogen microscopy by proton proton scattering*, Nucl. Instr. and Meth. B 197 (2002) 134-149.
39. Ina Reiche, Jacques Castaing, Thomas Calligaro, Joseph Salomon, Marc Aucouturier, Uwe Reinholz and Hans-Peter Weise, *Analyses of hydrogen in quartz and in sapphire using depth profiling by ERDA at atmospheric pressure: Comparison with resonant NRA and SIMS*, Nucl. Instr. and Meth. B 249 (2006) 608-611.
40. L.S. Wielunski, D. Grambole, U. Kreissig, R. Grötschel, G. Harding, E. Szilágyi, *Hydrogen depth resolution in multilayer metal structures, comparison of elastic recoil detection and resonant nuclear reaction method*, Nucl. Instr. and Meth. B 190 (2002) 693-698.
41. G.R. Rossman, *Hydrogen in "anhydrous" minerals*, Nucl. Instr. and Meth. B 45 (1990) 41-44.
42. Sparrow Corporation, http://www.sparrowcorp.com.
43. J.F. Ziegler, SRIM 2003, Version-2003.20. Available from http://www.srim.org.
44. N. Moncoffre, G. Barbier, E. Leblond, Ph. Martin, H. Jaffrezic, *Diffusion studies using ion beam analysis*, Nucl. Instr. and Meth. B 140 (1998) 402-408.
45. Carlos M. Castaneda, Thomas A. Cahill, Juan L. Romero, Roger S. King, *Depth profiling of hydrogen in amorphous media and applicable to quartz air filters*, Nucl. Instr. and Meth. B 145 (1998) 553-561.
46. Hans Keppler and Joseph R. Smyth, editors, *Water in Nominally Anhydrous Minerals,* Reviews in mineralogy & geochemistry, vol 62, 2006.
47. G.R. Rossman, *Studies of OH in nominally anhydrous minerals*, Phys. Chem. Minerals (1996) 23: 299-304.
48. J. Ingrin, H. Skogby, *Hydrogen in nominally anhydrous upper-mantle minerals: concentration levels and implications*, Eur. J. Mineral. 12 (2000) 543.
49. Erik H. Hauri, Glenn A. Gaetani and Trevor H. Green, *Partitioning of water during melting of the Earth's upper mantle at H_2O-undersaturated conditions*, Earth Planet. Sci Lett. 248 (2006) 715-734.
50. Akira Ito and Hiroko Koyama-Ito, *Possible use of proton CT as a means of density normalization in the PIXE semi-microprobe analysis*, Nucl. Instr. and Meth. B 3 (1984) 584-588.
51. J. Huddleston, I. G. Hutchinson, T. B. Pierce and J. Foster, *Development and comparison of techniques for two-dimensional analysis using the Harwell nuclear microprope*, Nucl. Instr. and Meth. 197 (1982) 157-164.
52. M. Cholewa, Yang Ping, Ng May Ling, Li Zhi Juan, H.O. Moser, Yeukuang Hwu, T.E. Gureyev, *High resolution 3-dimensional tomography with X-rays at Singapore synchrotron light source*, Nucl. Instr. and Meth. B 260 (2007) 45-48.
53. C. Rau et. al, *Synchrotron-based imaging and tomography with hard X-rays*, Nucl. Instr. and Meth. B 261 (2007) 850-854.
54. Jenny Svensson, Doctoral thesis, *Optical spectroscopy in biomedicine – detection of embedded inclusions and in vivo pharmacokinetics*, Lund Institute of Technology, Lund University, 2007.
55. Jonathan M. Lees, *Seismic Tomography of Magmatic Systems*, Journal of Volcanology and Geothermal Research (2007), doi: 10.1016/j.jvolgeores.2007.06.008

56. Avinash C. Kak, Malcolm Slaney, *Principles of Computerized Tomographic Imaging*, IEEE Press, New York, 1988, ISBN 0-87942-198-3.

57. Course material, Medical Image Analysis, TBMI45, Linköping University, http://www.imt.liu.se/edu/courses/TBMI45/pdfs/CT_Kap5.pdf (2007-09-10)

58. A. Sakellariou, M. Cholewa, A. Saint and G.J.F. Legge, *An accurate reconstruction algorithm for tomography experiments that involve complex probe-sample interactions*, Meas. Sci. Technol. 8 (1997) 746-758.

59. R. Gordon, *A tutorial on ART*, IEEE Trans. Nucl. Sci., NS-21, June 1974

60. G. Bench, K.A. Nugent, M. Cholewa, A. Saint and G.J.F. Legge, *Submicron STIM tomography reconstruction techniques*, Nucl. Instr. and Meth. B 54 (1991) 390-396.

61. S.C. Liew, I. Orlic, S.M. Tang, *PIXE tomographic reconstruction of elemental distributions using an iterative maximum-likelihood method*, Nucl. Instr. and Meth. B 104 (1995) 222-227.

62. Ryo Mimura, Hirosuke Takayama, Mikio Takai, *Nanometer resolution three-dimensional microprobe RBS analyses by using a 200 kV focused ion beam system*, Nucl. Instr. and Meth. B 210 (2003) 104-107.

63. F.A. Soldera, Y. Gaillard, M. Anglada Gomila, and F. Mücklich, *FIB-Tomography of Nanoindentation Cracks in Zirconia Polycrystals*, Microsc. Microanal. 13 (Suppl 2), 2007.

64. A. Sakellariou, D.N. Jamieson, G.J.F. Legge, *Three-dimensional ion micro-tomography*, Nucl. Instr. and Meth. B 181 (2001) 211-218.

65. A. Saint, M. Cholewa and G.J.F. Legge, *STIM tomography*, Nucl. Instr. and Meth. B 75 (1993) 504-510.

66. Physik Instrumente (PI) GmbH, Auf der Roemerstrasse 1, D-76228 Karslruhe, Available from http://www.pi.ws.

67. P. Formenti et al., *Heavy ion and proton beams in high resolution imaging of a fungi spore specimen using STIM tomography*, Nucl. Instr. and Meth. B 130 (1997) 230-236.

68. Robert MS. Schofield and Harlan W. Lefevre, *PIXE-STIM microtomography: zinc and manganese concentrations in a scorpion stinger*, Nucl. Instr. and Meth. B 72 (1992) 104-110.

69. G.S. Bench, A.J. Antolak, D.H. Morse, A.E. Pontau, A. Saint and G.J.F. Legge, *On the effect of beam spatial broadening in ion microtomography (IMT) image quality*, Nucl. Instr. and Meth. B 82 (1993) 447-458.

70. Claire Michelet, Doctoral thesis, *Développement d'une technique de micro-tomographie par faisceau d'ions a l'échelle cellulaire*, l'université Bordeaux I, 1998.

71. G.S. Bench and G.J.F. Legge, *High resolution STIM*, Nucl. Instr. and Meth. B 40/41 (1989) 655-658.

72. A.E. Pontau, A.J. Antolak, D.H. Morse, D.L. Weirup, *Minimum data set requirements for ion microtomography*, Nucl. Instr. and Meth. B 54 (1991) 383-389.

73. Stephen G. Azevedo, Daniel J. Schneberk, J. Patrick Fitch and Harry E. Martz, *Calculation of the Rotational Centers in Computed Tomography Sinograms*, IEEE Trans. Nucl. Sci 37, nr 4, 1990.

74. MATLAB®, Version 7.0.4.352, MathWorks Inc., Image Processing Toolbox.

75. Claire Michelet and Philippe Moretto, *STIM tomography at the cell level*, Nucl. Instr. and Meth. B 158 (1999) 361-367.

76. G. Bench, A. Saint, M. Cholewa and G.J.F. Legge, *STIM tomography: a three-dimensional high resolution imaging tool*, Nucl. Instr. and Meth. B 68 (1992) 481-490.

77. SKB Report, R-98-10, *Systemredovisning av djupförvaring enligt KBS-3*, SKB (Swedish Nuclear Fuel and Waste Management Co), 1998.
78. Ola Karnland & Martin Birgersson, Technical report, TR-06-11, *Montmorillonite stability*, SKB (Swedish Nuclear Fuel and Waste Management Co), 2006.
79. Hans-Rudolf Wenk and Andrei Bulakh, *Minerals: Their Constitution and Origin*, Cambridge University Press, 2004, ISBN 0 521 52958 1.
80. Ola Karnland, Siv Olsson, Ulf Nilsson, Technical Report, TR-06-30, *Mineralogy and sealing properties of various bentonites and smectite-rich clay minerals*, SKB (Swedish Nuclear Fuel and Waste Management Co), 2006.
81. R. Pusch, *Mechanical properties of Clays and Clay Minerals*, Ch. 6 Handbook of Clay Science, 2006, ISBN-13 978-0-08-044183-2.
82. N. Güngör, T.Tulun, A. Alemdar, *Determination of trace elements by instrumental neutron activation analysis in Anatolian bentonitic clays*, Nucl. Instr. and Meth. B 142 (1998) 550-560.
83. Harald Hökmark, *Hydration of the bentonite buffer in a KBS-3 repository*, Applied Clay Science 26 (2004) 219-233.
84. E. Gallucci, K. Scrivener, A. Groso, M. Stampanoni and G. Margaritondo, *3D experimental investigation of the microstructure of cement pastes using synchrotron X-ray microtomography (μCT)*, Cement and Concrete Research 37 (2007) 360-368.